2011

Evolution Of Microstructure And Residual Stress In Disc-shape Eb-pvd Thermal Barrier Coatings And Temperature Profile Of High Pressure Turbine Blade

Sriparna Mukherjee
University of Central Florida

STARS Citation
Mukherjee, Sriparna, "Evolution Of Microstructure And Residual Stress In Disc-shape Eb-pvd Thermal Barrier Coatings And Temperature Profile Of High Pressure Turbine Blade" (2011). *Electronic Theses and Dissertations, 2004-2019*. 1874.
https://stars.library.ucf.edu/etd/1874

EVOLUTION OF MICROSTRUCTURE AND RESIDUAL STRESS IN DISC-SHAPE EB-PVD THERMAL BARRIER COATINGS AND TEMPERATURE PROFILE OF HIGH PRESSURE TURBINE BLADE

by

SRIPARNA MUKHERJEE

M.S. Indian Institute of Technology, India, 2006

A thesis submitted in partial fulfillment of the requirements
for the degree of Masters of Science
in the Department of Mechanical, Materials and Aerospace Engineering
in the College of Engineering and Computer Science
at the University of Central Florida
Orlando, Florida

Summer Term

2011

Major Professor: Yongho Sohn

ABSTRACT

A detailed understanding of failure mechanisms in thermal barrier coatings (TBCs) can help develop reliable and durable TBCs for advanced gas turbine engines. One of the characteristics of failure in electron beam physical vapor deposited (EB-PVD) TBCs is the development of instability, named rumpling, at the interface between (Ni, Pt)Al bond coat and thermally grown oxide (TGO). In this study, thermal cycling at 1100°C with 1 hr dwell time was carried out on 25.4mm disc specimens of TBCs that consisted of EB-PVD coated ZrO_2-7wt. %Y_2O_3, (Pt,Ni)Al bond coat, and CMSX-4 Ni-based superalloy. At specific fraction of lifetime, TBCs were examined by electron microscopy and photostimulated luminescence (PL). Changes in the average compressive residual stress of the TGO determined by PL and the magnitude of rumpling, determined by tortuosity from quantitative microstructural analyses, were examined with respect to the furnace thermal cyclic lifetime and microstructural evolution of TBCs. The combination of elastic strain energy within the TGO and interfacial energy at the interface between the TGO and the bond coat was defined as the TGO energy, and its variation with cyclic oxidation time was found to remain approximately constant ~135J/m^2 during thermal cycling from 10% to 80% thermal cyclic lifetime. Parametric study at ~135J/m^2 was performed and variation in residual stress with rumpling for different oxide scale thicknesses was examined. This study showed that the contribution of rumpling in residual stress relaxation decreased with an increase in TGO thickness.

High pressure turbine blades serviced for 2843 hours and in the as coated form were also examined using electron microscopy and photostimulated luminescence. The difference in residual stress values obtained using PL on the suction and pressure sides of as-coated turbine blade were discussed. The presence of a thick layer of deposit on the serviced blade gave signals from stress free α-Al_2O_3 in the deposit, not from the TGO. The TGO growth constant data from the disc-shape TBCs, thermally cycled at 1100°C, and studies by other authors at different temperatures but on similar EB-PVD coated TBCs with (Pt, Ni)Al bond coat and CMSX-4 Ni-based superalloy were used to determine the temperature profile at the YSZ/bond coat interface. The interfacial temperature profiles of the serviced blade and the YSZ thickness profile were compared to document the variable temperature exposure at the leading edge, trailing edge, suction and the pressure side.

ACKNOWLEDGMENTS

I would like to express profound gratitude to my advisor, Dr. Yongho Sohn for his guidance and valuable suggestions.

I would like to take this opportunity to thank the members of my committee Dr. Jiyu Fang and Dr. Ming Su.

I acknowledge the cooperation and support of my laboratory members Prabhakar Mohan, Carmen Bargraser, Travis Patterson, Emmanuel Perez, Catalina Uribe, William Sprowes, Joshua Bush, Sarah Brennan, Youngjoo Park, Dongho Shin, Clara Hofmeister, Ashley Ewh, Judith Dickson, Katrina Bermudez, Ke Hung and Joseph Hamilton.

I am grateful to Dr. Ann Bolcavage from Rolls Royce Corporation and Dr. Ken Murphy from Alcoa Howmet Corporation for providing specimens required for this study.

Special acknowledgement is made to UCF's Materials Characterization Facility (MCF), Mikhail Klimov, Kirk Scammon and Karen Glidewell for providing technical help and arranging for equipment schedule.

And finally I sincerely appreciate the encouragement and love from my family and friends.

.

TABLE OF CONTENTS

LIST OF FIGURES

LIST OF TABLES

LIST OF ABBREVIATIONS

APS	Air Plasma Spray
CVD	Chemical Vapor Deposition
DS	Directionally Solidified
EB-PVD	Electron Beam-Physical Vapor Deposition
FEG	Field Emission Gun
FWHM	Full-Width Half-Maximum
GRAMS	Graphic Relational Array Management System
L	Roughened Length at TGO/bond coat interface
L_0	Flat Length at TGO/bond coat interface
LPPS	Low-Pressure Plasma Spray
PLS	Photostimulated Luminescence
PVD	Physical Vapor Deposition
RE	Reactive Elements
SEM	Scanning Electron Microscope
TBC	Thermal Barrier Coating
TCP	Topologically Close Packed
TGO	Thermally Grown Oxide
VPS	Vacuum Plasma Spray
XEDS	X-Ray Energy Dispersive Spectroscopy
XRD	X-Ray Diffraction
YSZ	Yttria Stabilized Zirconia

CHAPTER 1 INTRODUCTION

Residual stress in thin films and coatings formed using technical processes like sputtering and vapor deposition are commonly observed. An increase in the residual stress occurs during cooling when thermal expansion mismatch is present between the film and the substrate. TGO scale formed by diffusion of Al from the Al rich bond coat additionally develops stress. In this study the net compressive residual stress in the TGO scale was measured using a non destructive technique PLS.

Other known phenomenon from thermal cycling, at the TGO/bond coat interface is rumpling. Quantitative measurement of wrinkling of TGO scale on Fe-Cr-Al alloy using atomic force microscopy had been investigated by Tolpygo and Clarke [31]. For TBCs with YSZ top coat undulation on the surface of TGO scale cannot be determined using atomic force microscope. In this study rumpling is quantified using tortuosity and a novel method to measure rumpling from the cross-sectional back-scattered images has been proposed. Rumpling increases the interfacial area between the TGO and the bond coat. Also, a correlation between the two measurable parameters, rumpling and residual stress, was established. Rumpling was shown to reduce the residual stress in the TGO.

The interfacial energy and the elastic strain energy, from the residual stress, were combined and represented as TGO energy. TGO energy contained easily measurable terms, like TGO thickness, tortuosity and residual stress. A parametric study was performed on the TGO energy which revealed that the role of rumpling in the residual stress reduction decreases with an increase in the TGO thickness. This finding has significance because failure in the TBC results from the energy provided by elastic strain energy for damage initiation and propagation. However in the parametric study of TGO energy, the parameters were considered to be independent of each other. A more detailed study considering the correlation between different parameters is required.

The efficiency of turbines for industrial power plant and aero applications depends on the turbine inlet temperature. Due to the shape of the turbine blade, all the sections of the blade do not experience a uniform temperature. Temperature profiles of the three sections (inner, mid and outer) were computed using Arrhenius equation, derived from the experimental TGO growth rate constant and the growth rate constant data from literature. This gives an idea about the temperature at the interface of the YSZ and bond coat. To derive the surface temperature more information like the heat flux at the surface and thermal conductivity of the YSZ are required. The knowledge of interfacial temperature might indicate the effectiveness of the cooling system and help to optimize the efficiency of the turbine.

CHAPTER 2 LITERATURE REVIEW

2.1 Thermal Barrier Coatings

Aircraft and industrial gas turbine engines and steam turbines operate in aggressive environments involving high temperature and pressure, increased temperature gradients and large stresses. They are prone to erosion damage in the oxidizing and corroding atmosphere, and impact damage from particulate material ingested or created internally.

It becomes important to use materials with high mechanical strength and toughness at high temperatures and resistance to thermal shock, thermal fatigue, creep, chemical interaction, etc. There is no single material with all the mentioned properties; hence layers of materials with characteristic properties are used to improve the overall efficiency and durability of turbines. These systems are called thermal barrier coatings (TBC) and it comprises of four layers: the superalloy, bond coat, thermally grown oxide and the ceramic-top coat. For the optimum performance, the right balance between the constituents of a TBC system is very important [7, 12].

With advancement and research in TBC materials, modern gas turbine engines can use gas temperature 1650°C or higher. In jet engines, incoming air is compressed using compressor. This compressed air has high oxygen density and is mixed with fuel in combustor chamber and ignited. This causes an increase in the velocity and temperature of the air that causes the turbine to rotate, that in turn also rotates the compressor. The exhaust gas provides the necessary thrust for propulsion or generation of electricity. The individual components of the TBC system are discussed in more detail.

2.2 Superalloy

Superalloys are a metallic alloys whose creep, and fatigue strength are optimized for maximum load-bearing capability at temperature near their melting point (~1300°C) [2]. These are mostly Ni or Co based alloy. To minimize diffusive creep, the components are either produced as single crystals or directionally solidified (DS) with large grain size. Previous works have reported an increase in component life on changing the substrate structure from the conventional polycrystalline or DS to single crystal. Strengthening of superalloy is achieved using solid solution strengthening and precipitation strengthening mechanisms. Various elements like tungsten, molybdenum, aluminum, chromium are added as solid solution in the superalloy. Ni forms precipitate with aluminum (γ'-Ni_3Al) in γ-Ni matrix as shown in Figure 1.

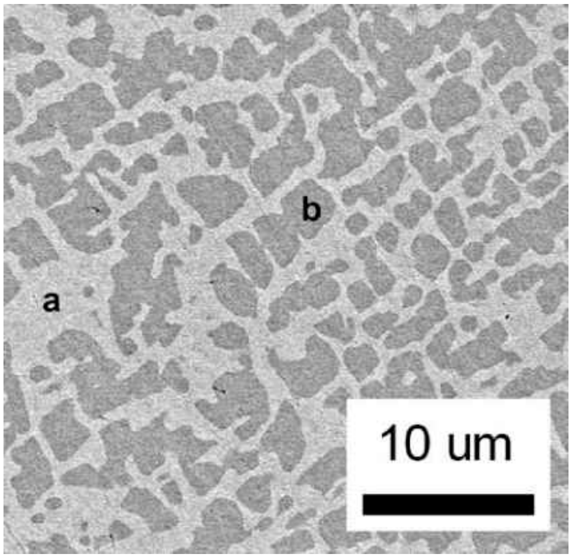

Figure 1: A typical microstructure of CMSX-4 Ni-based superalloy with γ' phase (b) in the γ matrix (a).

The advantages of adding aluminum is two fold, precipitation strengthening and oxidation resistance. Even though high Al content helps in the formation of uniform and adherent oxide layer, it is kept below 6wt. % to maximize creep strength and minimize the lowering of melting point. During oxidation depletion of Al reduces the fraction of γ' precipitates. Also similar issue exists with the Cr, corrosion resistant component of the superalloy. To retain the load-bearing capability of superalloy both Cr and Al contents are kept below that is required for corrosion and oxidation resistance. Therefore another, relatively thin, aluminum and chromium rich layer is required and this is called bond coat.

2.3 Bond Coat

This is a reservoir of aluminum and/or chromium. Most commonly applied bond coats are MCrAlY where M refers to Ni and/or Co; and intermetallic NiAl. Since the bond coat has Cr, Al and Ni; it is expected that there is a competition between these elements for the formation of their respective oxides. From the Ellingham diagram in Figure 2, Cr, Al and Ni are reactive to oxygen but Al oxide is the most stable. For alloys dilute in Cr and Al, the content of Al has to be greater than the critical limit with high diffusivity in the alloy for the formation of a continuous alumina layer [3, 4]. In addition, Figure 3 shows that alumina growth is the slowest process. Also, unlike Cr_2O_3, Al_2O_3 is not a volatile product. This also acts as an oxygen insulator. All these factors make Al_2O_3 the most desirable oxide. The only requirement remains is that a continuous and uniform layer of Al_2O_3 is formed. This is controlled by concentration of aluminum in the bond coat and its transportation to the interface. A uniform layer of Al_2O_3 deters the formation of transient oxides or the next stable oxides like chromium and nickel oxides. Bond coat can be applied using various methods.

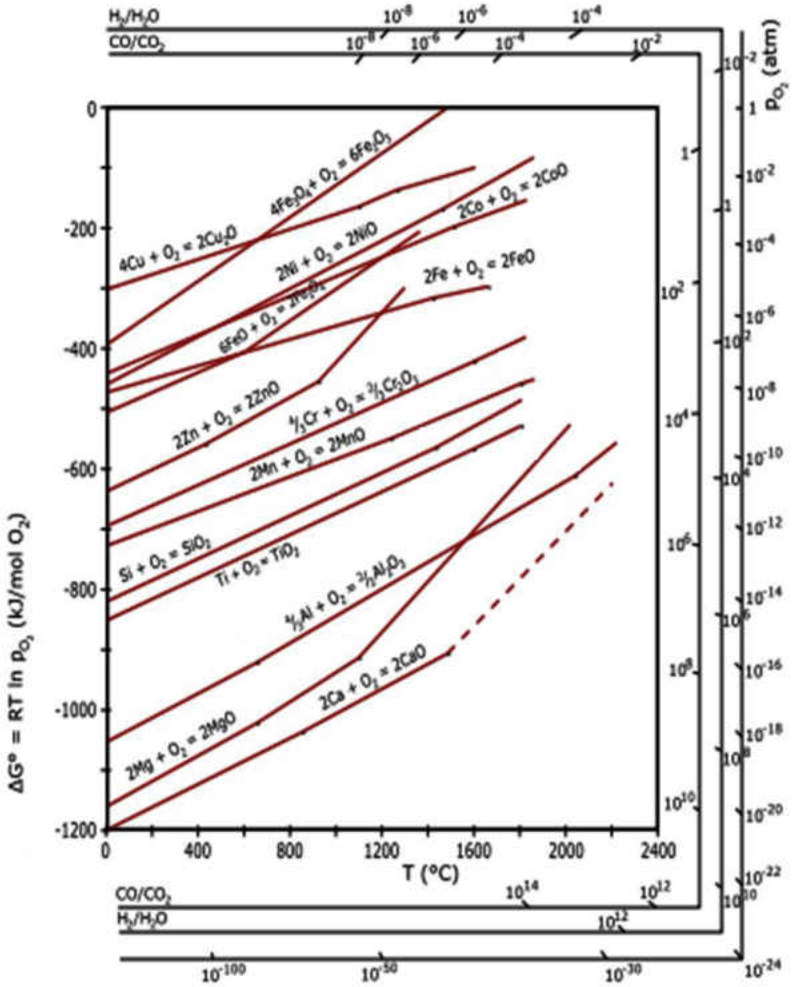

Figure 2: Ellingham diagram showing the stability of oxides at different temperature [41].

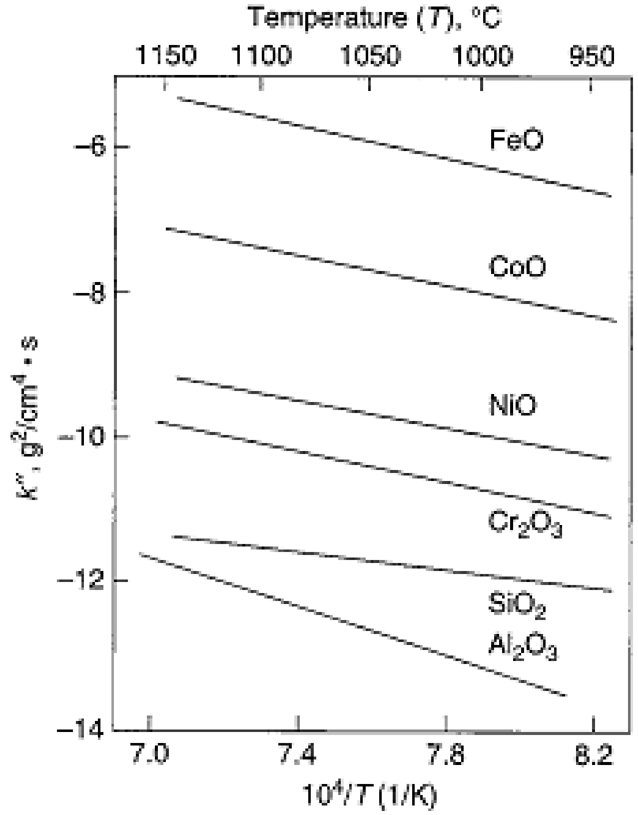

Figure 3: Parabolic rate constants for different oxides showing oxidation kinetics [42].

2.3.1 Aluminizing

This technique has been commercially available for many years. The steps involved in this process are: (a) formation of volatile species of Al, (b) transport of the vapors to the substrate acting as an aluminum sink, (c) displacement, disproportion and various reduction reactions at the surface of heated substrate to deposit elemental Al and (d) annealing to form desirable microstructure.

This can be further categorized as pack-cement process, above-the-pack process and chemical vapour deposition (CVD) process. The pack contains a powder source of Al, a halide activator and a filler. Filler is inert material that supports the component to be coated and forms uniform diffusion path of coating gas to the substrate in the pack-cement process. However potential problem of contamination from the pack material exist. Therefore in above-the-pack process the substrate is separated from the pack and the coating gas formed in the pack flows towards the substrate. In pack-aluminizing the activity of Al in the coating is determined by its activity in the source and the transport kinetics in the pack. The final microstructure of the coating will depend on the temperature and activity of Al in the source. High temperature and low activity of Al produces an outward growing coating and vice versa [1]. In pack-aluminizing, Cr and Al codeposition is difficult using independent sources. An alloy of the two elements is used that moderates the thermodynamic stability of Al halide vapor and increases the concentration of Cr in the vapor.

More control in the composition of coating vapor is possible using CVD process as shown in Figure 4 [5]. In this coating gases are generated externally and then introduced into evacuated retort containing the substrate.

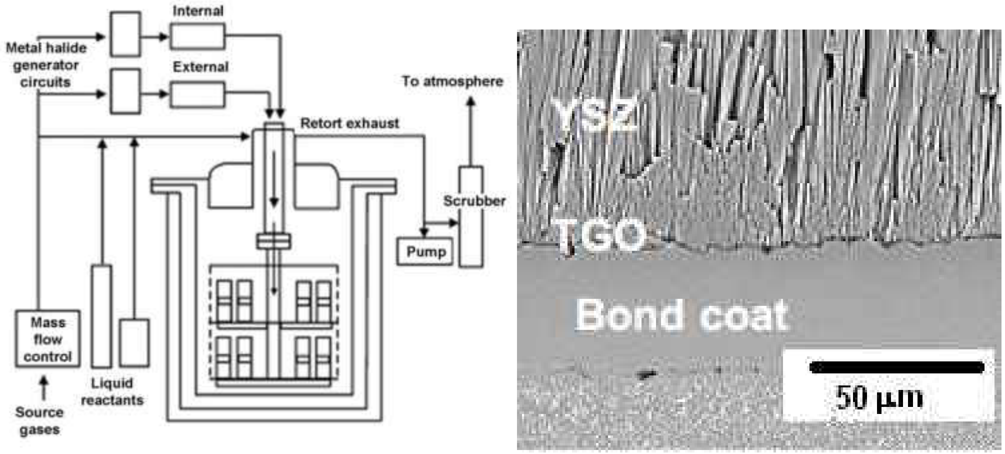

Figure 4: A schematic of Chemical Vapor Deposition technique for aluminide coatings and the resultant microstructure.

2.3.2 Overlay Coatings

Contrary to the diffusion coatings, the coating material is deposited onto the substrate and the adherence depends on the interaction at the coating and substrate interface. Small amounts of reactive elements (like Y, Hf etc.) that are difficult to deposit into diffusion coatings can be easily included in overlay coatings. Most commonly found overlay coatings are Ni–Cr–Al and Co–Cr–Al systems and are deposited using physical vapour deposition (PVD) techniques. The coating to be deposited is vaporized from the source pool under vacuum or low pressure using various heating methods like electron beam, electric-arc, laser beam source, induction heating, etc. Ingot is prepared by taking into consideration the relative vapor pressure of different components to be deposited. The vapor flows to the preheated substrate, as heating facilitates adhesion. This is followed by condensation, nucleation and growth of the bond coat on the superalloy. And finally the deposited bond coat is annealed to get the desired microstructure as shown in Figure 5.

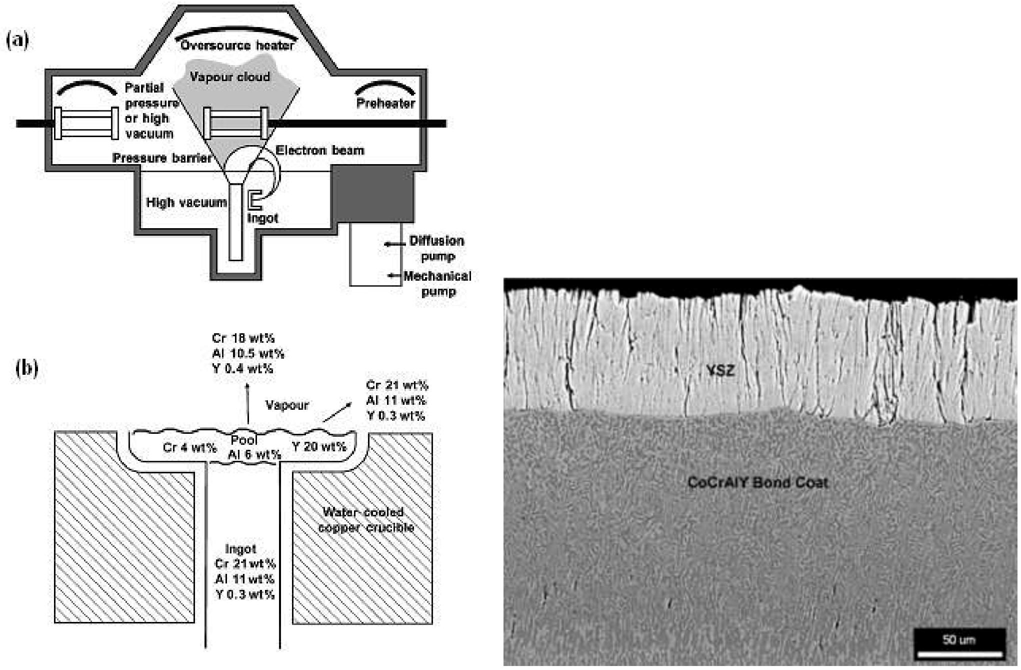

Figure 5: (a) A schematic of the EB-PVD chamber for deposition of CoCrAlY, (b) compositional variation between the ingot, pool and the vapor; and the resultant microstructure.

Another technique extensively used for deposition of an overlay coating is plasma spray process. In this technique the alloy in the form of powder is fed into the plasma gun, and the molten product is sprayed onto the substrate. Unlike other deposition techniques, this can also be carried out under atmospheric pressure as high rate of heat transfer and the short dwell time reduce the chances of oxidation of the metal particles. The temperature of the plasma can exceed 16,000ºC and the particle velocity can reach 200-300 m/s. However, relatively poor adhesion of the coating with the substrate can be observed. This is taken care of by the surface treatment of the superalloy by grit blasting that enhances the surface roughness. Coatings with reactive metals are deposited by vacuum plasma spray (VPS), low-pressure plasma spray (LPPS) or with the plasma shrouded with an inert gas, such as argon. In the plasma spray process a high voltage between the electrodes produces high temperature and high velocity plasma from excited primary gas and secondary gas mixture of argon or nitrogen and H_2. Simultaneously, powders of the coating material are either injected externally or internally into the plasma where they are liquefied and projected onto the substrate.

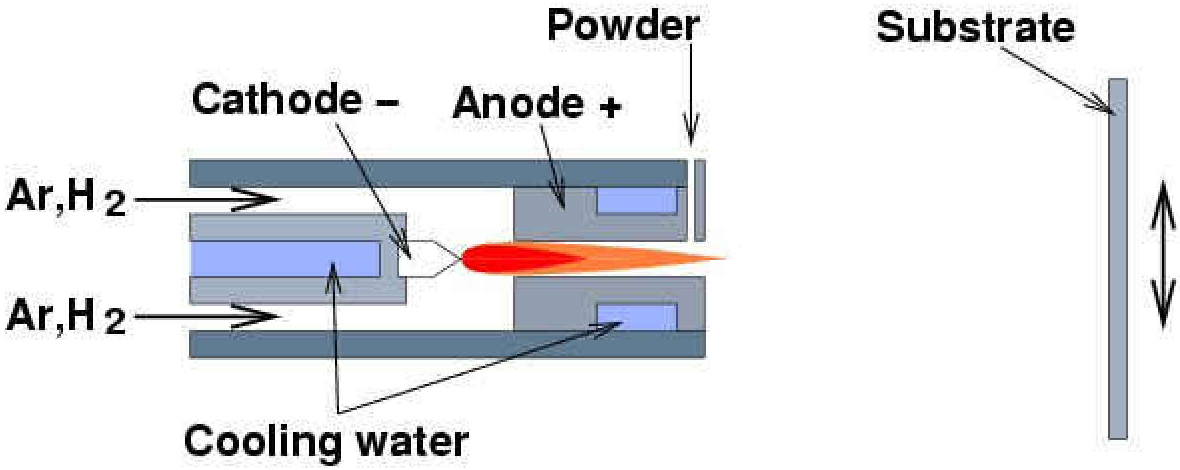

Figure 6: A schematic of the externally loaded Air Plasma Spray gun.

2.4 Ceramic Top Coat

A thermally insulating ceramic layer on the bond coat improves the efficiency of gas turbines by increasing the turbine inlet temperature or increase the durability by lowering the surface temperature of the bond coat. Use of ceramic coatings started from 1960's with the application of frit enamels and then Al_2O_3 and Zr_2O_3. These were not popular because of high thermal conductivity of alumina and destabilization of the zirconia-base materials. An ideal ceramic material should have high melting point, low thermal conductivity, high thermal expansion coefficient (close to that of the underlying metallic substrate), stable phase during entire operation, high oxidation and corrosion resistance and high strain tolerance. Low modulus of elasticity minimizes the residual stresses resulting from the mismatch of thermal expansion coefficient between the metallic coated substrate and the ceramic coating.

Based on these criteria Zr_2O_3 is the preferred material but has one issue that it undergoes a polymorphic phase transformation during heating and cooling [6]. The martensitic transformation at 1170°C on cooling zirconia causes 3-5% volume change that induces ~10% shear strain affecting the integrity of the coating [10]. Solid solution of zirconia with other oxides like CeO_2, CaO, MgO, Y_2O_3, Sc_2O_3 and In_2O_3 stabilizes the high temperature phase (tetragonal/cubic) and eliminates the volume change [7]. Y_2O_3 stabilized Zr_2O_3 (YSZ) is the most commonly used because of its low thermal conductivity with minimum temperature dependence [8, 4]. In addition very similar vapor pressure of Zr_2O_3 and Y_2O_3 simplifies the processing by vapor deposition. The industrial standard for Y_2O_3 content is ~7 wt %, because lower Y_2O_3 content does not inhibit the phase transformation, and higher amount stabilize a cubic phase, that has inadequate strength and toughness as shown in Figure 7. The transformable and non-transformable phases are depicted using the binary phase diagram of Zr_2O_3-Y_2O_3 shown in Figure 8. The YSZ also has a high thermal expansion coefficient of $11x10^{-6}$°C^{-1} comparable to that of the underlying metal (i.e.$14x10^{-6}$°C^{-1}). This produces fewer amounts of residual stresses resulting from the thermal expansion mismatch between the two layers.

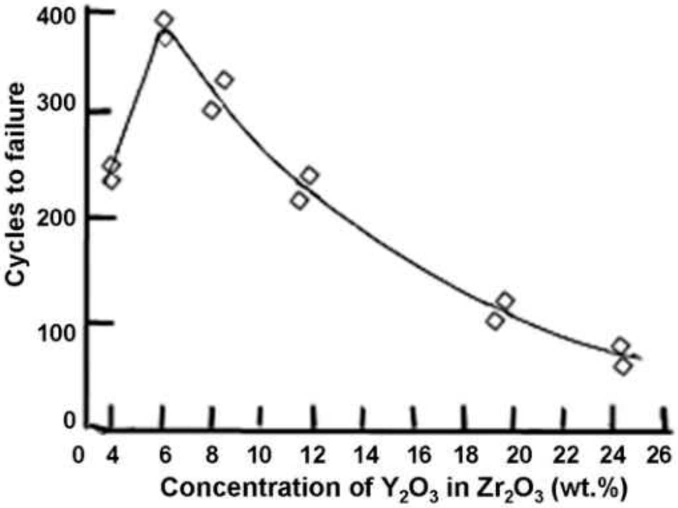

Figure 7: Durability of thermal barrier coating as a function of Y_2O_3 content [9].

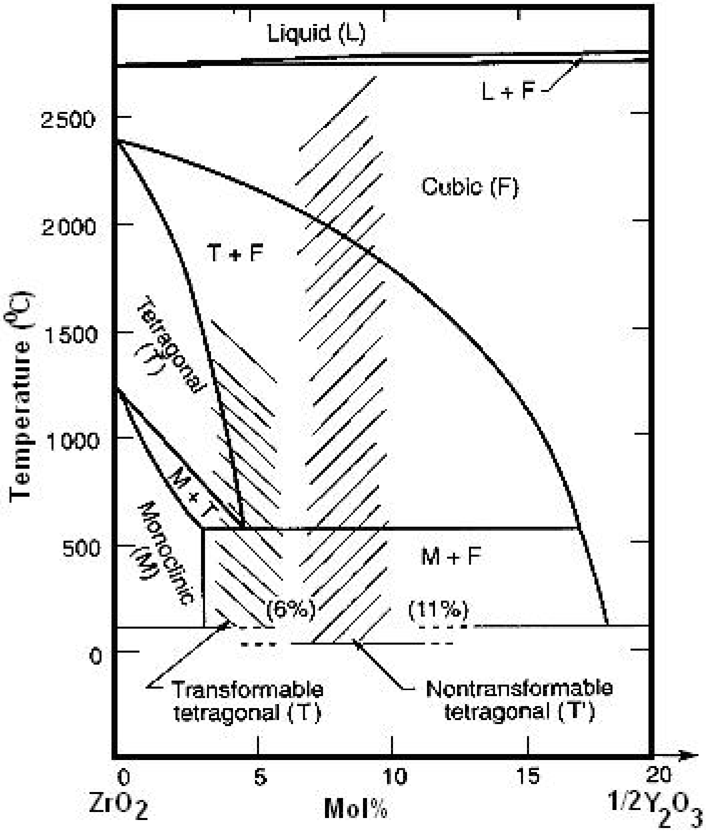

Figure 8: Equillibrium phase diagram of Zr_2O_3 and Y_2O_3 showing the Y_2O_3 stabilizer content range for the nontranformable tetragonal Zr_2O_3 (t'-phase).

Another essential property, the strain tolerance is imparted in the coating by two types of deposition techniques, air plasma spray (APS) and electron beam-physical vapor deposition (EB-PVD). Zirconia has a very high melting (~2700°C) that requires specific heating process like electron beam and plasma torch. Also, these processes provide the rapid quenching required for the formation of non-transformable t'-phase of the YSZ. Both techniques have been mentioned in previous section and the principles remain the same as for the deposition of bond coats. The two processes lead to coatings with different microstructures and in turn different thermo-physical properties.

The microstructure of coating formed using EB-PVD and APS techniques are shown in Figure 9 and Figure 10, respectively. In EB-PVD technique the deposition parameters are optimized to create columnar grains with microscale porosity. The bulk/fully dense Yttria stabilized Zr_2O_3 has thermal conductivity ~2.3W/mK due to phonon scattering by structural vacancies [11]. The gap between the columns in EB-PVD coated TBCs improves the strain tolerance and reduces the thermal conductivity to ~1.7W/m K. Another coating method, air plasma spray technique is used for coating turbines operating in less demanding conditions. The intersplat porosity and cracks in the ceramic coating are oriented parallel to the surface that further lowers the thermal conductivity to ~ 1.1W/m K. However APS ceramic layer has lower strain tolerance than EB-PVD TBCs. In both coatings, high porosity reduces the density of the coating which is a requirement for improving the performance of rotating components. The only limitation is that the linked porosity and the high oxygen diffusion expose the underlying bond coat to oxidation.

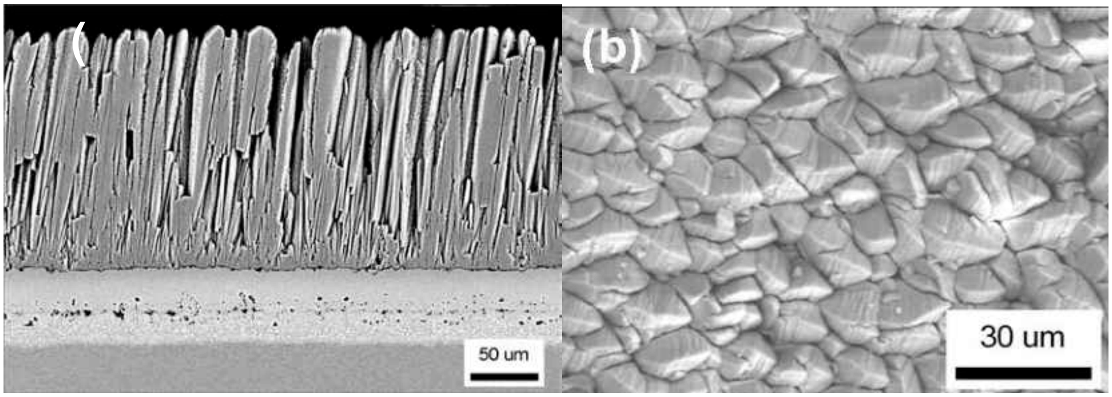

Figure 9: Back-scattered electron micrograph of the cross-section (a) and the scanning electron micrograph of the surface (b) of EB-PVD coated TBCs.

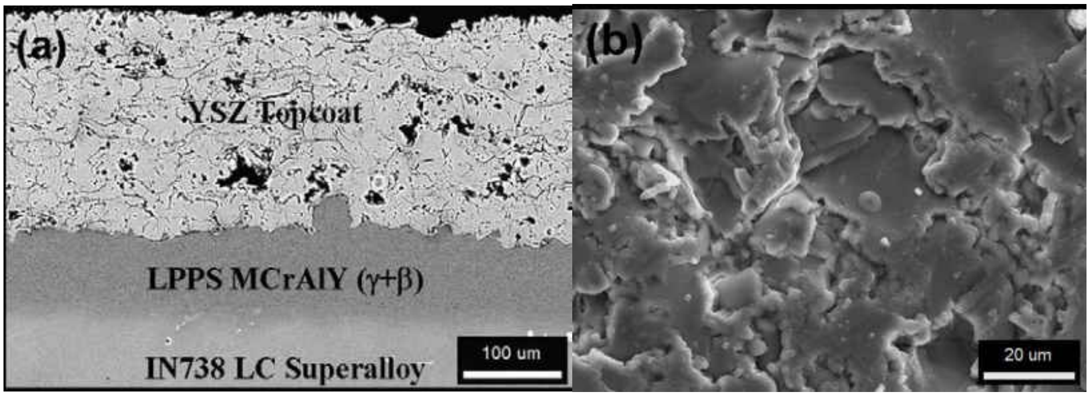

Figure 10: Back-scattered electron micrograph of the cross-section (a) and the scanning electron micrograph of the surface (b) of APS coated TBCs.

2.5 Thermally Grown Oxide

This is a reaction product of the bond coat oxidation. Among the various parameters that affect the chemistry and microstructure of the TGO scale; chemical composition of the metallic bond coat, oxygen partial pressure in the oxidizing atmosphere and the diffusion coefficients of both the oxygen and aluminum play significant roles. For alloys with Al content less than 15wt. % transient (Cr, Ni) oxides can form at lower temperature, however high temperature will result in stable Al_2O_3 phase since the diffusion coefficient of Al increases that increases the Al concentration at the bond coat surface. In the presence of ceramic coating, the TGO comprises of two distinct layers (a) equi-axed zone next to the top coat and (b) columnar zone close to the bond coat [19]. The constituent of the equi-axed zone depends on the type of bond coat. Some researchers have shown that the equi-axed zone on MCrAlY bond coat has Cr rich precipitates; and that on Pt-aluminide coatings have some amount of Zr_2O_3 [13]. Microstructure of the TGO affects the growth kinetics and the lateral strain within the oxide scale. A general understanding is that above 1200°C the α-alumina phase is the only oxide formed. And lower temperature causes θ- Al_2O_3 phase to form that subsequently transforms into α- Al_2O_3 with high temperature exposure time [14, 16, 18]. The rate of transformation depends on the temperature, surface texture and crystallographic orientation of the bond coat and its composition. It was suggested that Cr accelerated the transformation to α- Al_2O_3, while Pt stabilized θ- Al_2O_3 [15, 17]. The role of reactive elements in the transformation process is not very clear but some speculations are that Y_2O_3 stabilizes θ- Al_2O_3 phase [14].

The oxidation kinetics of the bond coat surface is monitored by measuring the TGO thickness with respect to the oxidation time. The thickness is a typically linear function of the square root of oxidation time where the rate-limiting step for oxidation is oxygen diffusion through the oxide. As expected the oxidation rate depends on the temperature (through Arrhenius relation). It also depends on the bond coat surface roughness. Faster TGO growth rate has been observed for grit-blasted bond coat compared to as-coated bond coat by some authors [19, 20, 21]. This is believed to be due incorporation of impurities from the grit blasting process into the oxide grain boundary during oxidation.

Grit blasting is found to provide nucleation sites (impurities and surface defects) for the formation of α- Al_2O_3 oxide instead of its metastable counterparts [22]. This causes oxide with smaller grain size to be formed and as the oxide growth is grain boundary diffusion process this leads to increased growth rate. L. Xie et al [23] have observed very small improvement in average life for grit blasted TBCs but proposed this to be an effective engineering solution as the variation in the spall life for sample from the same processing batch is little as shown in Figure 11. The role of bond coat surface treatment was extensively explored by I.T. Spitsberg et al [24]. After thermal cyclic treatment of EB-PVD TBCs on (Ni, Pt) Al bond coat with different types of surface treatments of the bond coat, she concluded that polished surfaces or the surfaces devoid of any imperfections enhances durability, and causes the TBC failure by different mechanism (i.e., edge delamination). Thus surface roughness becomes an important parameter when models are designed for estimating the life of TBCs.

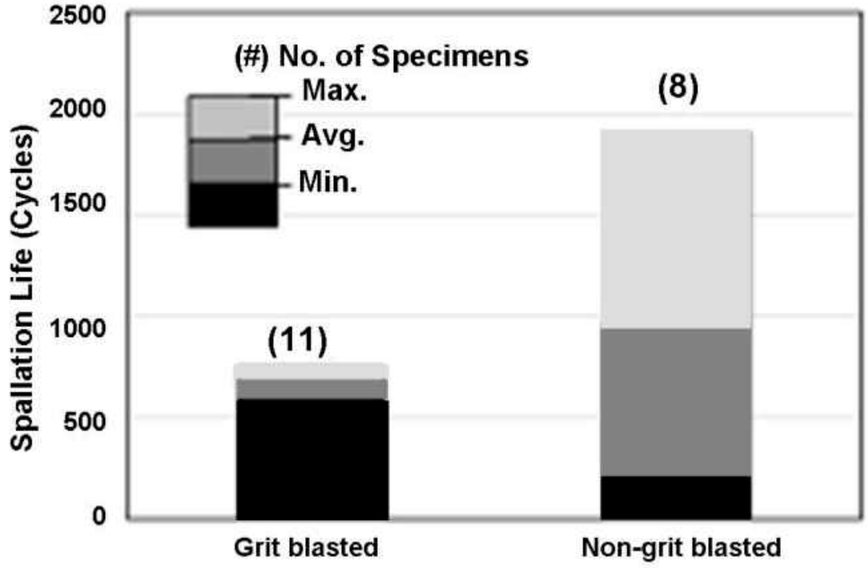

Figure 11: Effect of grit-blasted process on the spallation life of EB-PVD TBCs.

2.6 Photostimulated Luminescence Spectroscopy(PLS)

This is a non-destructive method for the determination of residual stress in the TGO scale. The high temperature XRD from the TGO scale shows compressive but small amount of the growth stress at the oxidation temperature. An approximate value of growth stress can also be obtained at room temperature by subtracting the computed thermal misfit stress from the net residual stress measured at ambient temperature. PLS is the most promising technique and is applied to measure the residual stresses in the α-Al_2O_3. Also the various polymorphs of alumina like θ-Al_2O_3 and γ-Al_2O_3 can also be identified. From XRD measurements at room temperature and PLS measurement of the oxide scale, the thermal misfit stress has been found to be compressive with magnitude in the range 2-6GPa [25]. PLS can be used at temperature below 600°C. Luminescence-peak broadening occurs at higher temperature. Also, because of the presence of top coat above the TGO scale, this technique cannot be applied to APS TBCs. The splat boundaries and microcracks are oriented normal to the incident laser. This obstructs the signal from the α-Al_2O_3 in the underlying TGO scale. On the contrary the columnar microstructure of EB-PVD coated TBCs provides unrestricted passage to the optical beam. However the thick YSZ column causes the laser to scatter and the probe size increases as the beam travels through the columnar top coat.

The origin of this technique started from 1970s and since many optimization methods have been carried out to get reliable and accurate stress values [26, 27]. Also it has been shown that systematic stress variation study of the TGO scale can be helpful in predicting the reliable remaining life of turbine blade [28]. As shown in Figure 12, in this optical technique, an external radiation source, argon ion laser, of wavelength 514 nm is used to excite Cr^{3+} impurity present in the α-Al_2O_3 within the TGO scale. The optically excited ion then release photons on returning back to a lower energy state. This luminescence can be recorded and correlated to the phases present and the biaxial residual stress in the TGO layer.

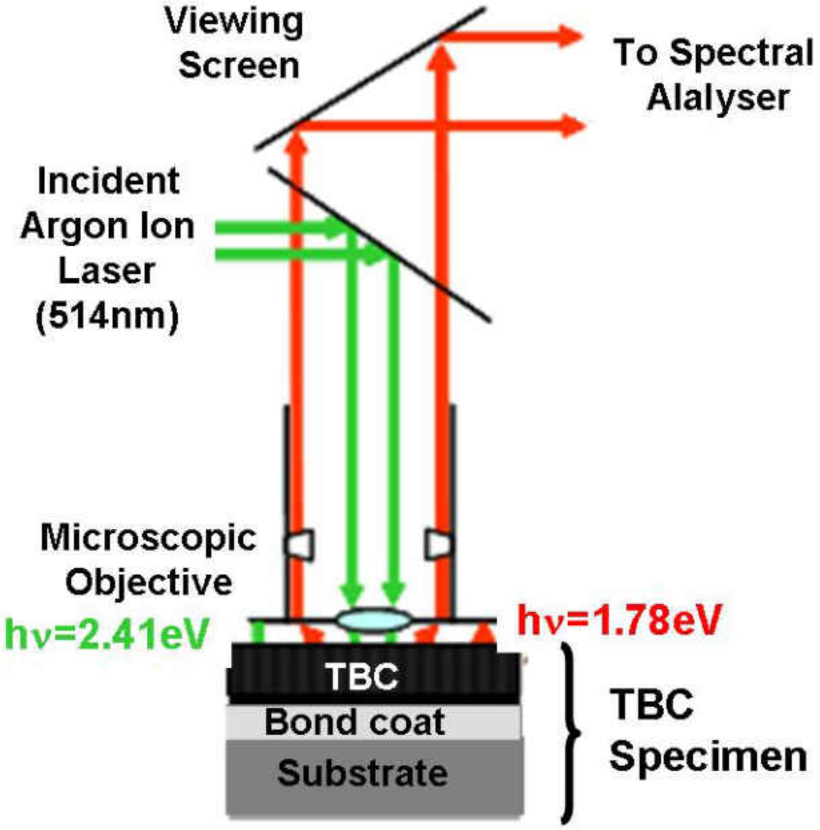

Figure 12: A schematic of the Photostimulated Luminescence Spectroscopy.

Two R_1 and R_2 fluorescence doublets at 14402 and 14432cm^{-1}, respectively, are obtained from the stress-free α-Al_2O_3. In the presence of stress, both R_1 and R_2 frequencies shift to a lower value as shown in Figure 13. Different aspects of the spectra were investigated to detect damage in TBC systems like the peak position (indicate the residual stress), peak width

(FWHM), peak shape (Gaussian Lorentzian mix), R_1-R_2 peak intensity ratio, the standard deviation of measured stress from location to location, and the fraction of measured peaks that can only be fit by two sets of R_1–R_2 peak pairs.

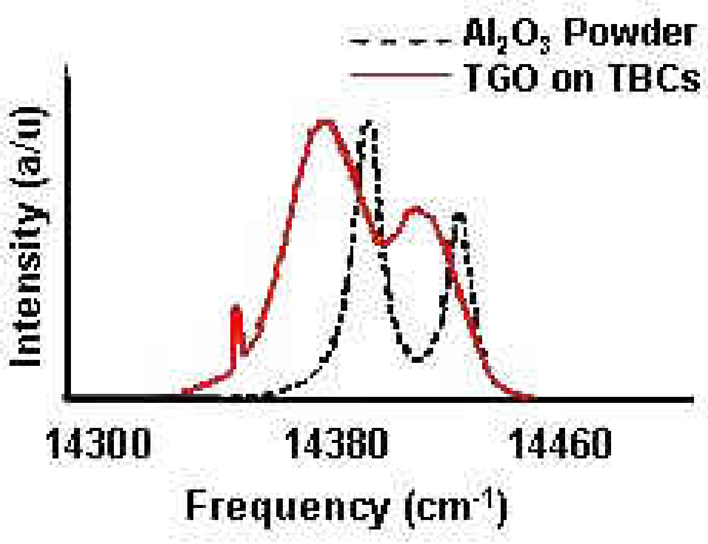

Figure 13: PSLS R_1-R_2 doublets for stress-free polycrystalline the α-Al_2O_3 and α-Al_2O_3 scale under compressive residual stress.

Systematic variation of peak shift with respect to life fraction, cycle time and exposure time; and its magnitude being larger than the instrumental noise makes this the most popular method for damage detection. A linear dependence of the peak shift of the R_2 line with stress is observed. Hence R_2 line is preferred over R_1 for stress measurement. The relation relating the frequency shift with residual stress is:

$$\Delta \nu_{\text{stress}} = \Pi_{ij}\,\sigma_{ij}^{c} = \Pi_{ij}\,a_{ki}a_{lj}\sigma_{kl} \tag{1}$$

The ijth component of the piezo-spectroscopic tensor is Π_{ij} and stress state in the crystallographic basis of the host crystal is σ^c_{ij}. The stress state is transformed into general coordinate system, σ_{ij}, using the transformation matrix, a_{ij}. The piezo-spectroscopic coefficient was measured (7.6$cm^{-1}GPa^{-1}$) by He and Clarke [29], and the off-diagonal terms were taken as zero. In his study he used a single crystal of ruby containing 0.05 wt. % of Cr^{3+}. Uniaxial compressive stress was applied along one of the three principal crystallographic directions and corresponding frequency shift was measured. The stress was varied to 0.9GPa and the diagonal terms of the piezo-spectroscopic tensor were calculated from the slope of the linear curve between the frequency shift and the applied stress.

The Eq. (1) is averaged over all the crystallographic directions for probe volume larger than the size of a single grain in an untextured polycrystalline TGO scale. The resultant equation then relates the piezospectroscopic shift to the hydrostatic component of the stress:

$$\overline{\Delta\nu} = \frac{1}{3}\Pi_{ii}\,\sigma_{jj} \tag{2}$$

Eq. (2) was modified for in-plane equi-biaxial stress condition and the final equation can be expressed as:

$$\overline{\Delta\nu} = \frac{2}{3}\Pi_{ii}\,\overline{\sigma} = 5.07(\mathrm{cm^{-1}GPa})\overline{\sigma} \tag{3}$$

There is also effect on the piezospectroscopic shift from the concentration of Cr^{3+}, given by:

$$\Delta\nu_{\mathrm{conc}} = 0.99 \,*\, c_{\mathrm{Cr}} \tag{4}$$

An increase in the amount of Cr^{3+} in the TGO scale has an opposite effect to that from an increase in stress [30, 31]. The presence of impurity in the oxide scale increases the creep rate of the scale. Due to an increase in the creep of the oxide scale, residual stress relaxation is observed, and this will decrease the piezospectroscopic shift closer to the stress free α-Al_2O_3 [32]. Also R_1 and R_2 luminescence lines have a temperature dependence 0.15 $cm^{-1}K^{-1}$ [27]. So the cumulative effects on the piezospectroscopic shift from the above three factors can be summed up as:

$$\Delta v = \Delta v_{\text{conc}} + \Delta v_{\text{stress}} + \Delta v_{\text{temp}} \tag{5}$$

2.7 Failure Mechanisms

Understanding of the failure mechanism operating in the TBCs is necessary to determine the life prediction mode. However a complex interplay between different layers, their continuously changing chemistry and thermo-physical properties and subsequently mixed mode of failure, makes the task difficult. Failure mechanism depends on a number of factors: (a) the type of the bond coat; MCrAlY and Pt-aluminide coatings have distinct failure mechanism, (b) the microstructure of the top coat, APS fails differently from the EB-PVD TBCs, (c) the thermal history of the application, industrial turbines and aero-engines fail differently and surface treatment of the bond coat prior to the deposition of the top coat. Industrial turbines are operated for longer period with few cycles, very close to isothermal conditions. The aircraft engines are operated at full capacity for short duration with frequent cycles.

One of the failure mechanisms commonly observed in TBCs with Al depleted bond coat is the formation of spinels (Co,Ni)(Cr,Al) and α-Cr_2O_3 at the interface of the TGO. As oxidation occurs, the Al content of the bond coat decreases and leads to formation of mixed oxides. The spinels are brittle and forms site for the initiation of cracks.

Most commonly failure is related with the growth of the TGO at high temperature and thermal strains generated by the thermal expansion mismatch upon cooling and heating. The oxide forming constituents, oxygen and aluminum diffuse along the grain boundary of the oxide at oxidation temperature. When reaction happens along the boundary normal to the interface, growth stress is observed but reaction at the interface leads to solid body displacement of the oxide scale without stress as illustrated in Figure 14 [33]. TBC effective life is guided by a sequence of crack nucleation (caused by the residual stress or foreign object damage), propagation and coalescence, and finally failure by large-scale buckling or spallation.

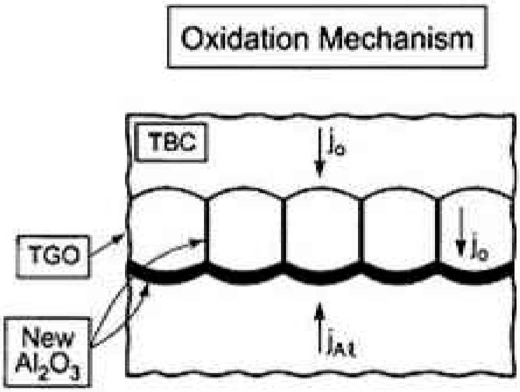

Figure 14: A schematics of proposed mechanism of the oxide growth; and the lengthening and thickening of the TGO.

P.K. Wright et al. [34, 35] explained the buckling spallation of TBCs using fracture mechanics. For a given residual stress in the TGO, the TGO critical thickness for which the strain energy release rate per unit area of crack equals the fracture toughness is given by

$$h_c = \xi * \left[E_0 \Gamma^{I}_{i} \Big/ \sigma^2_0 (1-\nu) \right] \tag{6}$$

The ξ is greater than 1, this implies that only a portion of the strain energy is used for crack initiation. σ_0 is the in-plane residual stress in the oxide; ν and E_0 are the poisson ratio and the elastic modulus of the oxide scale, respectively. Γ^{I}_{ι} (J/m^2) is the mode I interface toughness.

For the validation of any mechanism, definition of critical quantities that provides the criterion for occurrence of the event using that particular mechanism is necessary.

In particular, for buckling failure, the sequence of steps leading to failure is illustrated schematically in Figure 15. An example is shown in Figure 16 for buckling and spalling of thermally-grown Al_2O_3 scale on Fe–Cr–Al heat-resisting alloy [36].

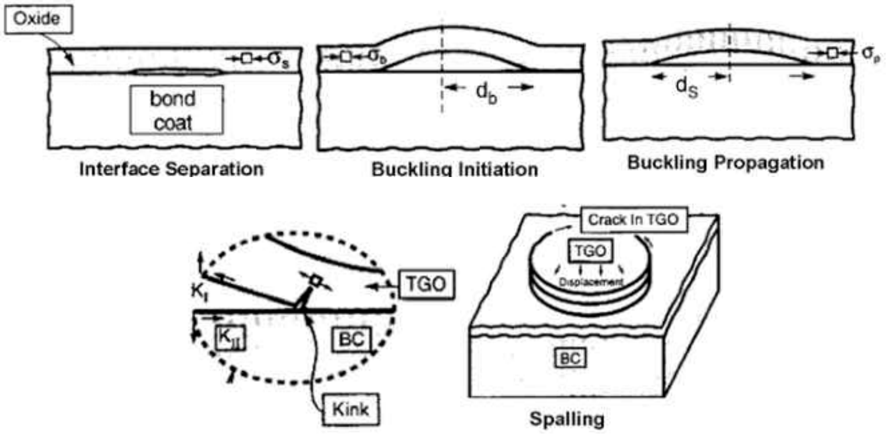

Figure 15: A schematic illustration of the stages of buckling and spalling involving (a) interfacial separation, (b) buckling, (c) kinking and (d) spalling.

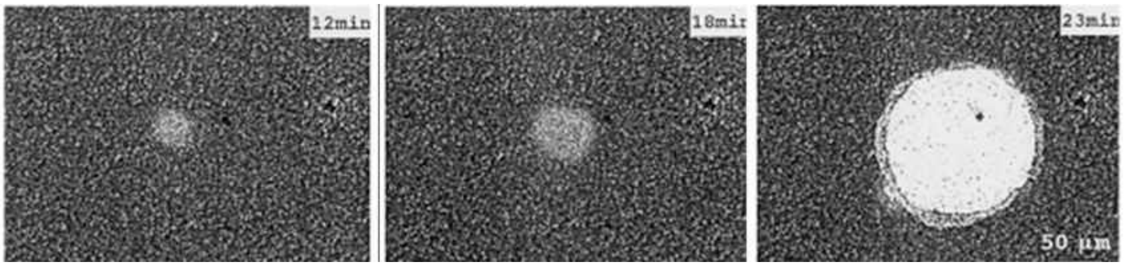

Figure 16: Sequence of optical images showing the buckling and spalling of thermally-grown alumina film on Fe–Cr–Al heat-resisting alloy. The incipient buckle grows at room temperature leading to sudden spalling after 23 mins exposing the bare bond coat.

The detail of the individual steps is as follows [35].

(a) As expressed by Eq. (6), for the film to separate along the weakly bound interface, a critical value of stress and critical film thickness is required.

(b) The critical separation (d_b) of the film, for buckling to happen is given by Eq. (7). Thus, for a given stress and thickness of the film, d_b represents the minimum separation that buckles.

$$d_b = 2.2h\sqrt{E_0/\sigma_0} \tag{7}$$

The buckle will spread since the energy release rate increases, but this leads to mode mixity effects as shown in Figure 17. As the size becomes larger than d_b, the relative proportion of mode II to mode I increase sharply and this increases the interface toughness. Here, Ψ is the mixity angle, where $\Psi = 0$, refers to mode I and $\Psi = \pi/2$, refers to mode II.

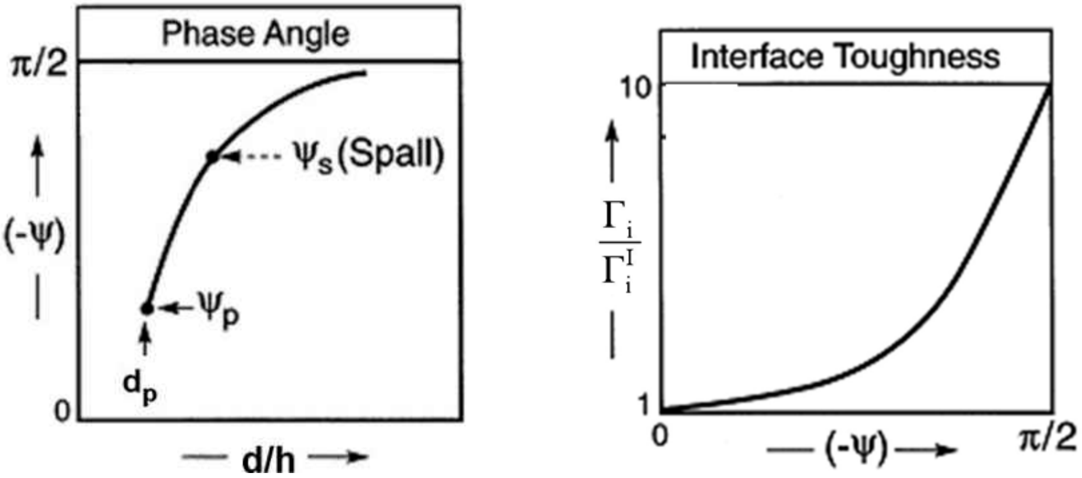

Figure 17: The mode mixitity effect on propagation of buckling.

(c) The final failure will depend on the deflection of the interface crack into the film resulting in dynamic spalling. The spalling event will strongly depend on the mode mixity and the ratio of the interface toughness to the oxide toughness. The kinking criterion is given by [36]:

$$d_s \approx 2.2h \;\exp[0.7(\Gamma_{ox}/\Gamma_i^I)\text{-}1.25]\sqrt{E_o/\sigma_o} \qquad (8)$$

From the above equation, it is clear that $d_s = d_b$ for $\Gamma_i^I / \Gamma_{ox} \geq 0.56$. This indicates that for very tough interfaces, kinking occurs as soon as the film buckles. If the interface toughness is low then the buckle propagates and then the kinking will depend on the mode mixity. However the tendency for kink increases as the buckle propagates.

In conclusion for the film to be in the fail safe condition, the oxide thickness has to be less than h_c and the separation size has to be less than d_b. For typical elastic moduli and film compression levels, d_b will be about 20 h or more. A relatively large interface flaws is required for the start of buckling in the absence of any surface imperfections. This signifies the role of imperfections on the nucleation of buckling delaminations. J.W. Hutchinson and coworkers [37] explained the effect of imperfections (mainly wrinkles) using both analytical and numerical method. Two types of imperfections are depicted in Figure 18. In the nucleation step, the oxide energy release rate increases and reaches a peak value (G_{peak}). Then there is a decrease in energy release rate that reaches an asymptote. This causes the interfacial flaw to arrest. Then in the propagation step of buckling, if this flaw size is the critical buckling size, there is an increase in the energy release rate leading to a steady state G_{ss} value. In the case of imperfections like wrinkles, the size of the imperfection will determine the initial separation for buckling. There is a critical size above which buckling failure will take place or else the separation will simply arrest.

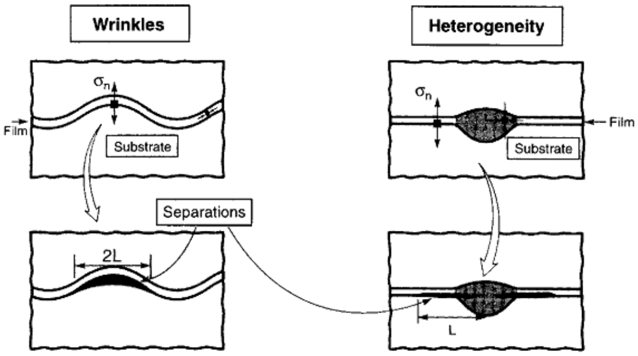

Figure 18: Schematics of the nucleation of flaw at the imperfections. Two typical imperfections in the thermal barrier coating systems are shown.

Presence of Y_2O_3 and $Y_3Al_5O_{12}$ (yttria-alumina garnet YAG) in the oxide of TBCs causes morphological heterogeneities since localized increase in the diffusion of oxygen is observed. These heterogeneities serve dual purpose, initiation of crack and on the contrary forms attached ligaments of film that enhances durability. Pt aluminide does not contain Y, so mostly wrinkles initiates separation of film from the substrate in these TBCs.

Along with buckle delamination, another mechanism for thin film failure is edge delamination. The differences in the appearance of two samples spalled by the two different mechanisms (buckle and edge) are shown schematically in Figure 19.

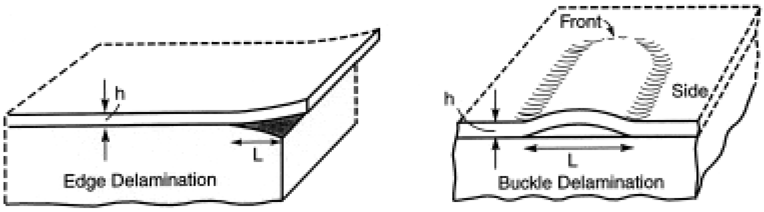

Figure 19: Schematic illustration of two types of delaminations: (a) Edge and (b) Buckling.

Unlike buckle failure, the edge delamination needs an initial flaw close to the edge. Also, the interface separation for edge delamination spreads as modeII. In thin film edge delaminations are relatively less common due to high level of mode II interfacial toughness and the resistance from frictional force at the interface.

The spallation behavior of TBC depends on the configuration of the oxide-metal interface. Upon cooling from the oxidation temperature, a flat oxide develops biaxial compressive stress σ_0 given by:

$$\sigma_0 = E_{ox}\varepsilon_T/(1-\nu_{ox}) \tag{9}$$

In Eq. (9), ε_T is the misfit strain, E_{ox} and ν_{ox} the Young's modulus and Poisson ratio of the TGO. The oxide growth stress is not included as its value is low due to stress relaxation at high temperature. Undulation or wrinkling of the oxide and the oxide-metal interface produces tensile stresses at the convex areas and at the valley the interface is under compression [35, 39]. The tensile stress at the crest leads to interface separation and initiate failure as shown in Figure 20. The inclined sections of the interface between the crest and the valley experience shear stress as shown in Figure 21. The normal and shear stresses are given by:

$$\sigma_{ij}/\sigma_0 = (A/L)Q_{ij}(\alpha_D, h/L) \tag{10}$$

These depend on wavelength of the undulations L, their amplitude A and the thickness of thermally grown oxide h. The function Q_{ij} depends on the Dundurs' parameter α_D and h/L. The Dundurs' parameter is given by [38]:

$$\alpha_D = (\overline{E}_{ox} - \overline{E}_s)/(\overline{E}_{ox} + \overline{E}_s) \tag{11}$$

In Eq. (11), $\overline{E}_{ox}$ and $\overline{E}_s$ are the plane strain modulus of the film and substrate, respectively.

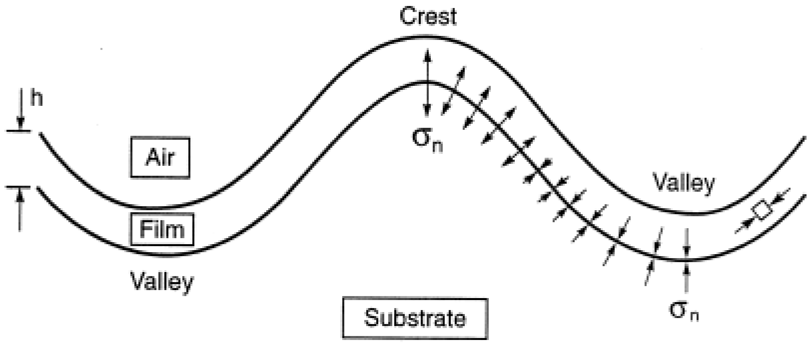

Figure 20: A redistribution of residual stress around an undulation causing tensile stress at the crest and compressive stress at the valley.

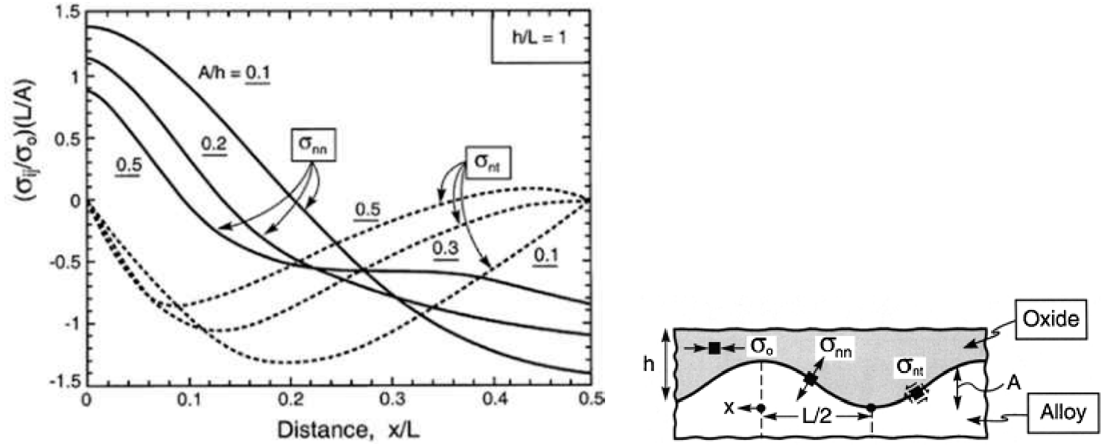

Figure 21: A variation in the magnitude of normal and shear stress along an undulation. At the crest and valley the normal stress levels are high and shear stress is zero. But at the inclined surface the magnitude of shear stress increases.

The gradual bond coat and oxide interface roughening (also named rumpling, ratcheting or undulation instability) occurs in the aluminide and MCrAlY bond coatings primarily during thermal cyclic oxidation with a periodic temperature change between ambient and higher than 1100°C operating temperature. A number of reasons for this gradual increase in the rumpling parameters (amplitude and wavelength) with thermal cycling have been proposed using theoretical models and numerical simulations. Some of the explanations are: (a) the cyclic plastic strains (creep or yielding) in the bond coat due to residual stress in the oxide scale [40], (b) coating and substrate thermal expansion mismatch and (c) martensitic transformation in aluminide bond coats during cooling and heating cycles. Failure from ratcheting is common for EB-PVD TBCs with grit blasted aluminide bond coat. For TBCs with top coat, an increase in amplitude of undulation causes tensile stress in the top coat. This leads to cracks parallel to the interface as shown in Figure 22. The plastic strains in the bond coat is introduced both during heating and cooling, however an intrinsic asymmetry between the plastic response to tension and compression produces definite amount of plastic strain with each cycle and may result in roughening of the bond coat surface.

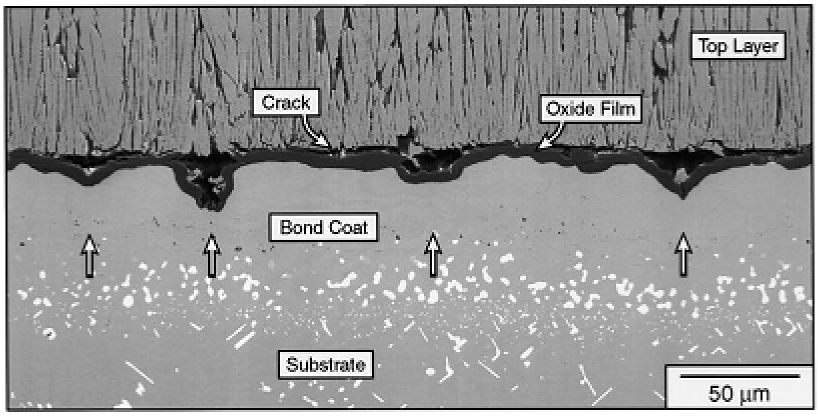

Figure 22: Ratcheting phenomenon and failure in the EB-PVD coated TBCs with aluminide bond coat. White arrows indicate the depressions in the bond coat [40].

According to work by I.T. Spitsberg and her coworkers [24] the failure of TBCs strongly depends on the surface treatment of the bond coat. In aluminized bond coats, ridges are observed at its grain boundaries. These ridges promote redistribution of the in-plane stress. The initial separation due to normal tensile stress at the interface is characteristic to the shape of the ridges as shown in Figure 23.

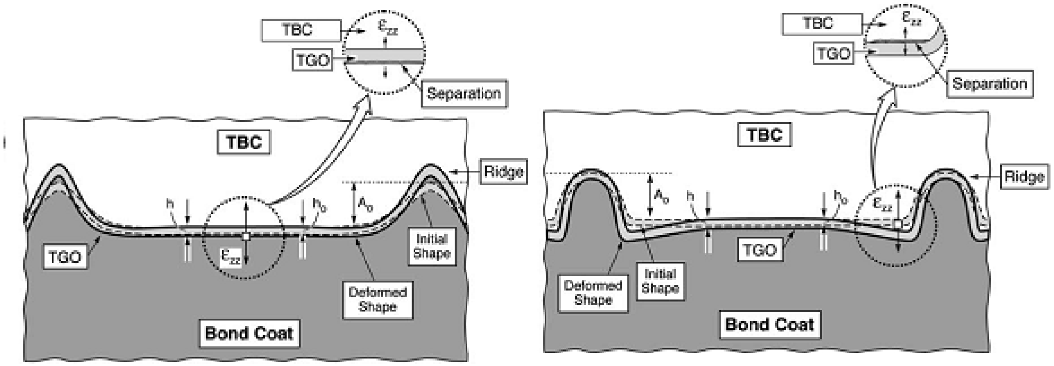

Figure 23: Schematics depicting the possible failure initiation modes for as-aluminide bond coated EB-PVD TBCs.

CHAPTER 3 PHENOMENOLOGICAL DESCRIPTION OF TGO ENERGY

The α-Al_2O_3 in the TGO contains in-plane compressive residual stress, measured using the photostimulated luminescence spectroscopy (PLS), at ambient temperature. This stress has two components; the dominant one is the thermal mismatch stress that results on cooling to ambient temperature and other is the lateral growth stress due to oxidation kinetics at high temperature. The magnitude of the thermal mismatch stress from previous studies on different coating systems is generally 3-6GPa [25] and that of oxide growth stress is less than 1GPa [45]. The residual stress in the TGO is present as strain energy. Undulation of the TGO and TGO/bond coat interface decreases the residual stress in the oxide scale by increasing the lateral dimension to accommodate growth and thermal mismatch strain. But this increases the TGO/bond coat interfacial area hence the interfacial energy.

Undulation is a fundamental source of failure in TBC with (Ni,Pt)Al bond coat. These undulations grow in amplitude and the requirements for its steady-state growth based on prior simulations and observations are [3, 40, 46] (a) preexistent ridges and imperfections at the topcoat/bond coat interface, (b) cyclic thermal history, (c) compressive stress in the TGO on cooling due to the thermal expansion misfit between the TGO and substrate compressions (d) cyclic yielding of the bond coat, (d) decreased reverse cyclic yielding of bond coat due to growth strain in each cycle and (e) creep in the TGO and bond coat. The residual stress undergoes redistribution near imperfections at the TGO/ bond coat and TGO/topcoat interfaces leading to out-of-plane stresses. Theses out-of-plane stresses and the energy provided by the elastic strain energy causes crack initiation, propagation and final failure of TBC.

In this study the strain energy in the TGO and TGO/bond coat interfacial energy is collectively defined as the TGO energy. To understand the equation of the TGO energy, a schematic is used that is shown in Figure 24. This illustrates the growth strain and thermal misfit strain in the TGO accrued in a cycle and subsequent development involving undulation. For simplicity the first oxidation cycle of the as coated specimen is shown. Figure 24(a) shows the as coated specimen with relatively planar interface and a very thin TGO scale with a residual compressive stress. The thermal expansion coefficient of TGO is 8.5 x 10^{-16} $°C^{-1}$ and is lower than that of the bond coat which is 16 x 10^{-16} $°C^{-1}$ [47]. At high temperature thickening and lateral growth of the TGO takes place. Only lateral growth contributes to the in-plane residual stress and is represented as ε_g. On cooling again due to difference in thermal expansion coefficient with the bond coat a thermal misfit strain, ε_t develops in the TGO. Note that both ε_g and ε_t are not elastic strains. Now in Figure 24(b) the TGO is assumed to be detached from the substrate so the total unconstrained strain in the TGO is expressed by:

$$\frac{\Delta L}{L_0} = \varepsilon_g + \varepsilon_t \tag{12}$$

However in real systems, the TGO experiences restrain from the underlying bond coat and a part of the unconstrained strain will convert into elastic strain that is what is measured using PLS. The remaining strain $\frac{L - L_0}{L_0}$, shown in Figure 24(c) will appear as rumpling at the TGO/bond coat interface as shown in Figure 24(d) where L is the roughened length at the TGO/bond coat interface and L_0 is the flat length of the interface. In this study it is assumed that the area of the bottom surface of the TGO in Figure 24(c) does not change on rumpling and is very similar to the TGO/bond coat interfacial area in Figure 24(d).

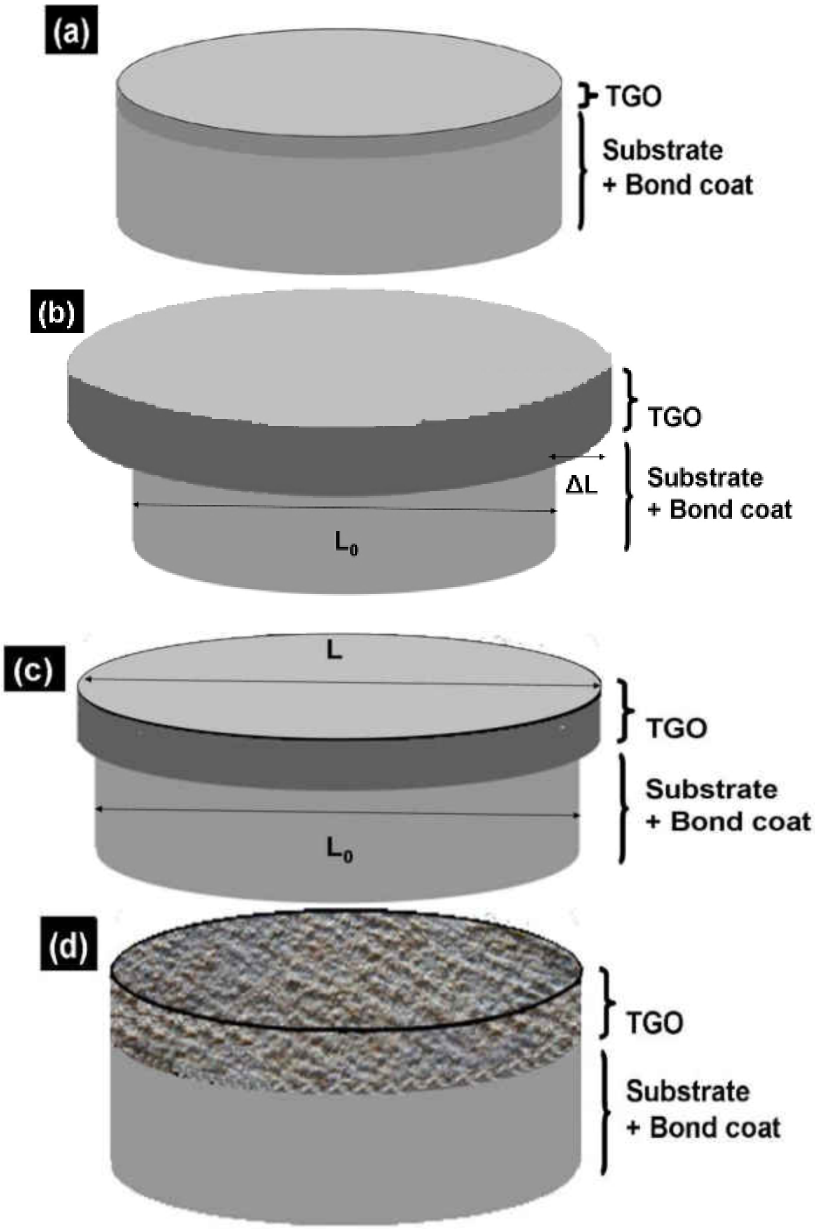

Figure 24: A schematic illustration of thermal mismatch, growth strain and rumpling: (a) as coated specimen with thin layer of oxide, (b) after single cycle of thermal oxidation without restraint from the substrate, an hypothetical situation depicting the lateral strain ΔL (combination of thermal misfit and growth strain, note: theses are not elastic strain), (c) the remaining strain (L-L_0) after some part of ΔL converts to elastic strain and (d) actual situation where the remaining strain is manifested as rumpling.

The EB-PVD disc specimens at different fraction of lifetime were employed for image analysis. These were cut at the center and the flat cross-sectional length (L_0) corresponded to the diameter of the disk specimen. Hence the flat surface area can be represented using:

$$\text{Flat surface area (m}^2\text{)} = \frac{\pi L_0^2}{4} \tag{13}$$

The actual interfacial area is undulated and the calculation of this area involves many geometrical parameters representing the roughness at the TGO/bond coat interface. To simplify this as mentioned before it is assumed that the area in Figure 24(c) is similar to the undulated interfacial area and is given by:

$$\text{Interfacial area (m}^2\text{)} = \frac{\pi L^2}{4} \tag{14}$$

The elastic strain energy per unit area in a film of thickness h is given by [48, 49]:

$$\text{Strain energy (J/m}^2\text{)} = \frac{\sigma^2 (1-\nu) h}{E} \tag{15}$$

In Eq. (15), the elastic residual stress in the TGO is σ and L is the roughened length at the TGO/bond coat interface. Material properties of the TGO incorporated are Young's modulus E and Poisson's ratio ν having values 390GPa and 0.22 respectively [50]. Thus the total elastic strain energy in the TGO film is expressed by:

$$\text{Strain energy (J)} = \frac{\sigma^2 (1-\nu) * \pi L^2 h}{E * 4} \tag{16}$$

Also the interfacial energy is given by:

$$\text{Interfacial energy (J)} = \frac{\gamma_{\mathrm{MO}} * \pi L^2}{4} \tag{17}$$

where γ_{MO} is the interfacial tension at α-Al_2O_3/bond coat interface whose value is taken as $7 J/m^2$ [4].

As mentioned earlier the combination of strain energy in Eq. (16) and interfacial energy in Eq. (17) was termed as the TGO energy in this study. This TGO energy was given by:

$$\text{TGO energy (J)} = \frac{\sigma^2(1-\nu) * \pi L^2 h}{E * 4} + \frac{\gamma_{\mathrm{MO}} * \pi L^2}{4} \tag{18}$$

On diving both sides with the flat surface area as described in Eq. (13), the Eq. (18) reduces to:

$$\text{TGO energy (J/m}^2\text{)} = \frac{\sigma^2(1-\nu)h}{E} * \left(\frac{L}{L_0}\right)^2 + \gamma_{\mathrm{MO}} * \left(\frac{L}{L_0}\right)^2 \tag{19}$$

Eq. (19) is a critical part of this study. This relates the TGO energy with easily measurable parameters like TGO thickness h, TGO's residual stress σ and the TGO/bond coat tortuosity (L/L_0). This was applied to understand the evolution of TGO energy with thermal cycles.

CHAPTER 4 EXPERIMENTAL DETAILS

4.1 Specimen Description

EB-PVD TBC systems in two forms were investigated in this study. One form was a disc of diameter 25.4mm and thickness 8mm as shown in Figure 25; and the other was in the shape of airfoil with flat length of 25.4mm from the leading edge to trailing edge (Figure 26).

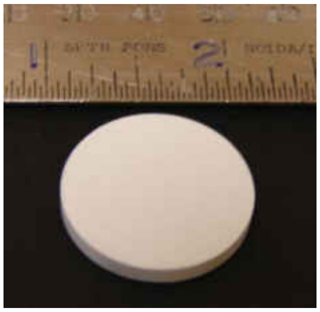

Figure 25: Optical photograph of as-coated EB-PVD TBC along with an inch scale.

The disc specimen as well as the airfoil comprised of an EB-PVD 8wt. % Y_2O_3-stabilized ZrO_2 coating (top coat) on (Ni, Pt)Al bond coat; deposited by a commercially known technique named MDC-150L that involves electroplating a thin layer of Pt onto the substrate followed by low activity aluminizing chemical vapor deposition (CVD) process; on a single crystal of Ni-based CMSX-4 superalloy substrate.

The thickness of top coat in the disc specimen was 179µm and that of the bond coat was 32µm. The nominal composition of CMSX-4 superalloy substrate in wt. % is Ni–57.7Co–9.9Ta–6.9W–8.3Cr–6.1Al–6.1Re–3.04Ti–0.9Hf.–0.8. Grit blasting of (Ni, Pt)Al bond coat with fine corundum particles (~220 grit Al_2O_3 at 20-30 psi) prior to the deposition of the YSZ leads to a very rough surface with less prominent β-(Ni, Pt)Al grain-boundary ridges but numerous surface imperfections like sharp edges, craters, and microcracks.

In the case of the blade, two types, as-coated and the serviced, each in three sections were received; and these sections were called outer, middle and inner sections (Figure 26). The serviced blade had undergone 2842 hours of engine operation and had yellow-orange coloration possibly due to the presence of deposit as shown in Figure 27. The variable curvature of the blade from leading edge to the trailing edge led to non uniform top coat thickness throughout the blade ranging from 110µm–178µm.

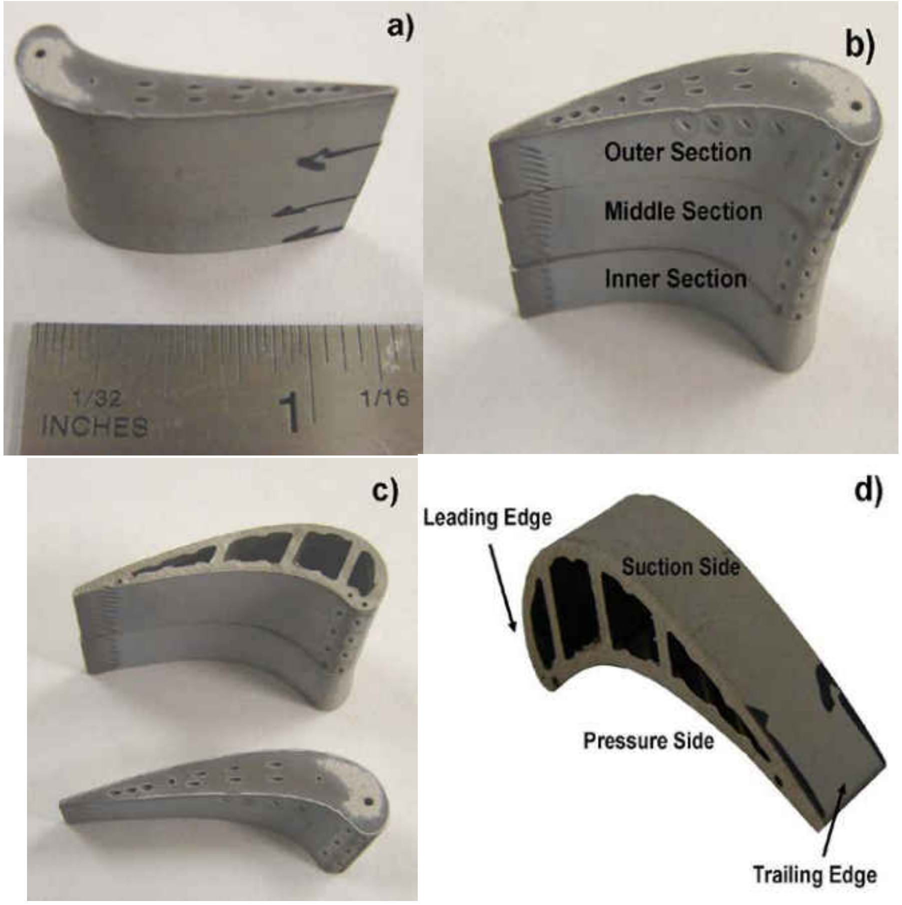

Figure 26: Optical photographn of as-coated airfoil depicting: (a) Suction side and, (b) Pressure side with different sections, (c) air channels and (d) terminologies for airfoil.

Figure 27: Optical photograph of serviced blade coated completely with colored deposit.

4.2 Lifetime Evaluation

Thermal cycling lifetime of the disc specimens of TBCs was evaluated using CM Rapid High Temperature Furnace with a thermal cycle consisting of 10 minute ramp up to 1100°C, 1 hour dwell at 1100°C and subsequent 10 minute rapid fan cooling as shown in Figure 28. Rapid heat up rates were achieved using molydisilicide heating elements Kanthal Super 1800 and temperature of the specimen was monitored using Type "S" thermocouple attached to the specimen stage. Thermal cycling was carried out and failure was declared when 70% of the coating was detached from the substrate. Average thermal cycle lifetime of the specimen was determined based on the life of three similar disc specimens.

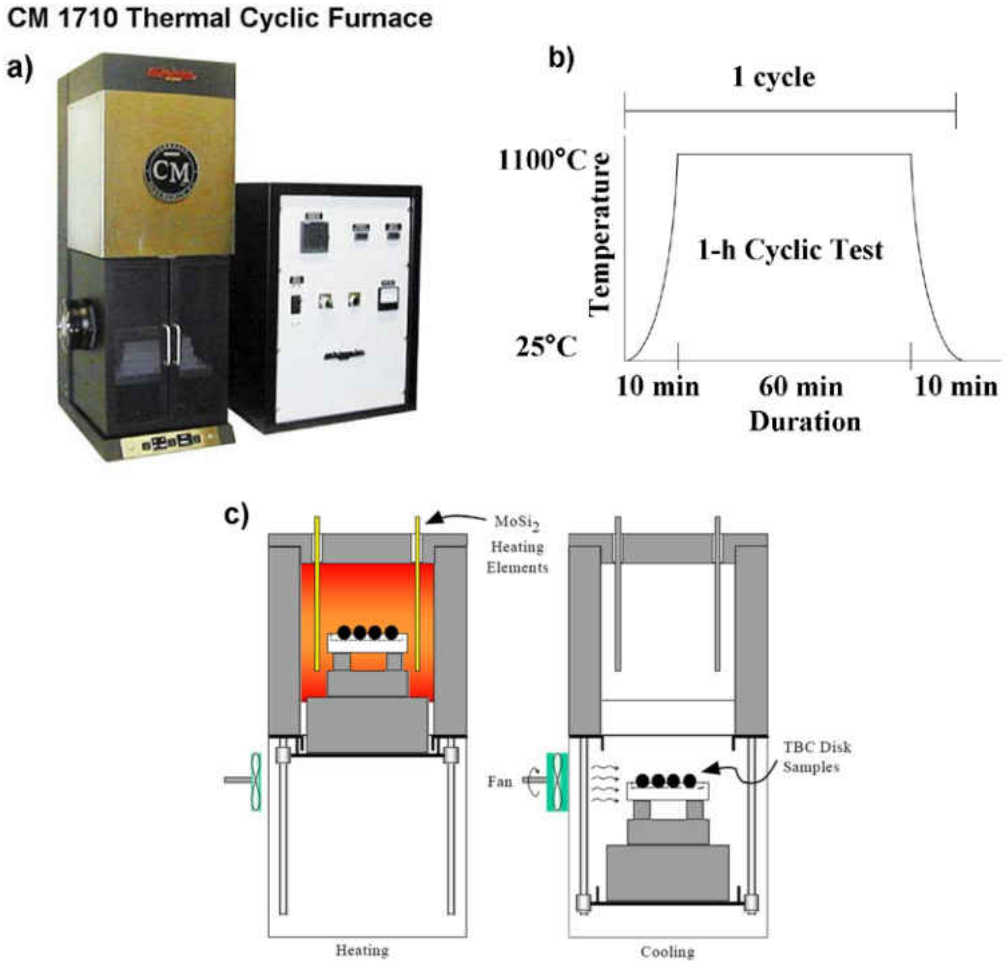

Figure 28: Photograph of the thermal cyclic furnace (a); and schematics showing the heating and cooling involved in each cycle (b) and(c).

4.3 Residual Stress Estimation in the TGO

The magnitude of compressive residual stresses; and the polymorphs of alumina in the TGO were examined using a non destructive technique, photostimulated luminescence spectroscopy (PLS). The as-coated specimen, specimens after 5%, 10%, 30%, 50% and 80% of lifetime and failed sample were cooled to room temperature prior to the experiment. Evolution of the residual stress with the thermal cycles (5%, 10%, 30%, 50% and 80% lifetime) was monitored till the failure of the sample. Average value of stress was calculated from 20 measurements covering the whole sample. A Renishaw^{TM}, System 1000B Ramanscope^{TM} (Renishaw^{TM}, Gloucestershire, UK) with a Leica^{TM} DM/LM optical microscope as shown in Figure 29 was employed for PL analysis that uses a 514nm argon-ion laser as probe and receives a spectrum from Cr^{3+} impurities in the TGO scale. Before and after each experiment, the spectrometer was calibrated by taking a spectrum of a strain-free sapphire crystal that exhibited R_1 and R_2 luminescence peaks at 14402cm^{-1} and 14432cm^{-1} respectively. De-convolution of the PL spectrum was carried out using Graphic Relational Array Management System (GRAMS) by fitting mixed Gaussian and Lorentzian function with a quadratic background. Since the luminescence spectrum comprises of R_1–R_2 doublets, a set of peaks were assigned; based on constraints on R_1 and R_2 relative intensity ratio, frequency separation, peak shape, width and height ratio (listed in Table 1) as proposed by Selcuk and Atkinson [27].

Table 1: Description of list of constraints applied for peak fitting.

Type of Constraint	Permissible Range
Lorentz factor R_1	0.55 – 0.90
Lorentz factor R_2	0.2 – 0.6
Intensity ratio H_{R1}/H_{R2}	1.4 – 1.8
Full width at half maxima ratio W_{R1}/W_{R2}	1.0 – 1.4
Peak separation ν_{R2}-ν_{R1}	$29\text{cm}^{-1} – 34\text{cm}^{-1}$
Goodness of fit	0.98 – 1.00

Figure 29: Renishaw^{TM} Photostimulated luminescence spectrometer.

4.4 Microstructural Analysis

Thermal cyclic oxidation was performed on the disc-specimens. The evolution of microstrustural features such as TGO scale thickness and rumpling was monitored as a function of oxidation time. For both airfoil and disc, surface morphology, cross-sectional phase constituents and compositions were analyzed using scanning and back-scattered electron microscope (Zeiss ULTRA-55 FEG SEM) and X-ray energy dispersive spectroscopy (XEDS) (Noran System 7) respectively.

4.4.1 Sample Preparation

The surface topography of specimens was observed using scanning electron spectroscopy after sputter coating the surface with a thin layer of Au-Pd to form a conductive surface that prevents charging. For imaging of the cross-section, all specimens were mounted in epoxy prior to cutting with a Buehler™ Isomet™ low speed diamond saw. The final preparation of cross-section of the sample involved grinding and polishing using SiC pads and diamond paste respectively prior to sputter coating with Au-Pd.

- Disc-specimen

The surface features, cross-sectional microstructure and chemical constituents of as-coated sample, samples after 5%, 10%, 30%, 50% and 80% lifetime and failed sample were examined using SEM and XEDS. The mode of fracture was determined by examining at the underside of the surface of spalled coating and the bare bond coat using SEM and XEDS.

- Airfoil

The middle section of the as-coated airfoil was cut into half and cross-sectional SEM was performed on the one with the leading edge after mounting it in the epoxy (Figure 30). All three sections of the serviced blade were mounted and examined under SEM.

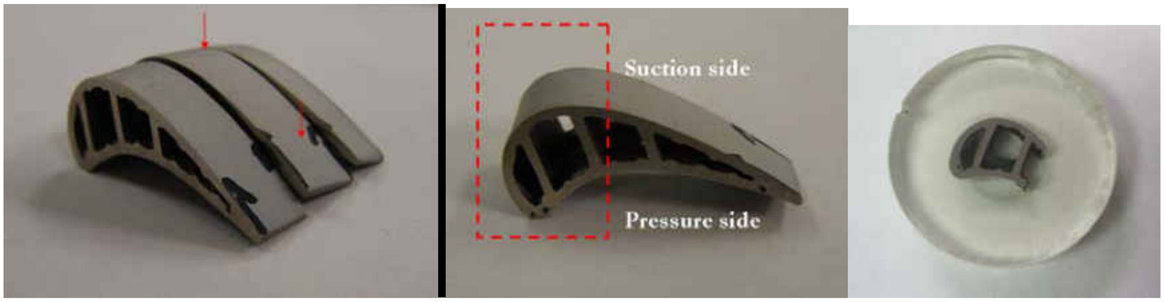

Figure 30: Sample preparation of as-coated airfoil for cross-sectional SEM.

The high-resolution imaging and compositional image analysis was performed using Zeiss ULTRA-55 equipped with Silicon Drift XEDS Detector. It uses Schottky field emission source and can achieve 1nm resolution at 15KV. For this study, imaging was performed using voltage 20–25KV.

4.4.2 Measurement of TGO Scale Thickness

Image analysis of the cross-sectional back-scattered micrographs was performed using IQmaterials^{TM}. The spatial calibration was performed for each image using the reference micron bar within the image. Average TGO thickness was calculated using 5 measurements from each of the ten backscattered images taken covering the entire specimen.

4.4.3 Measurement of Roughness of the TGO/Bond Coat Interface

Undulation at the TGO/Bond coat interface was characterized by tortuosity, that is the ratio of length of roughened interface to the flat length expressed by:

$$\text{Tortuosity} = \frac{\text{Roughened Length}\,(L)}{\text{Flat Length}\,(L_0)} = \frac{\text{Perimeter} - (\text{Side 1} + \text{Side 2} + \text{Flat Length})}{\text{Flat Length}} \qquad (20)$$

Based on the average amplitude roughly (5μm) and wavelength roughly (30μm), all images were taken at 500X magnification to include at least three undulation features per micrograph. Image editing was required prior to the tortuosity measurement. A uniformly colored region, in this case the bond coat, was selected and painted white using image editing software Paint.Net and the interface was enclosed in a rectangular box with line width 1 pixel as demonstrated in Figure 31. This confined white area that was considered as a particle for which perimeter was obtained using IQmaterials^{TM}. The three straight line lengths when subtracted from the perimeter gave the roughened length of the interface. Average rumpling was computed at varying oxidation fraction from 20 measurements on each specimen.

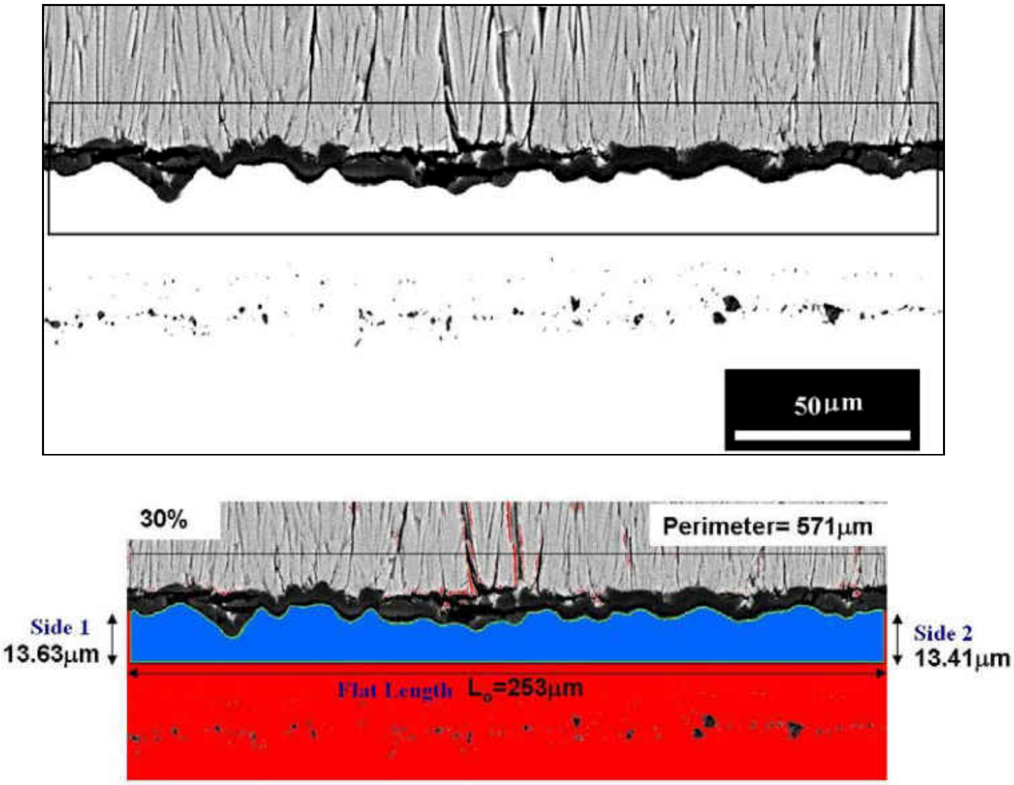

Figure 31: Rumpling measurement procedure sequence demonstrated using a cross-sectional image of 30% lifetime EB-PVD TBC.

CHAPTER 5 RESULTS

5.1 Disc-Shape EB-PVD TBC Specimens

5.1.1 Characterization of As-coated EB-PVD TBC Specimens

Scanning electron micrograph of the surface of the top coat shown in Figure 32 and backscattered electron micrographs of the cross-section shown in Figure 33(a) indicate a typical EB-PVD microstructure with columnar grains and channels between the grains. The top coat is ~180μm thick and the EDX spectrum of this region presented in Figure 34(a) shows that it comprises mostly of ZrO_2. A very thin layer of the TGO scale (~ 0.42 ± 0.1μm) was observed at the interface between the YSZ and (Ni, Pt)Al bond coats with roughness characteristic of a grit blasted bond coat. The EDX spectrum of the embedded Al_2O_3 from the grit blasting of the superalloy prior to the deposition of the bond coat is presented in Figure 34(d). The back-scattered electron micrograph of the embedded Al_2O_3 is shown in Figure 33(c). The bond coat is ~32μm thick and the EDX spectrum, presented in Figure 34(b) indicates that it is Pt modified NiAl. Also ~22μm thick interdiffusion zone comprising of intermetallic phases and topologically close packed (TCP) phases was observed between (Ni, Pt)Al bond coat and CMSX-4. The EDX spectrum of the superalloy, presented in Figure 34(c), shows that it is Ni-based alloy with alloying elements (Co, Cr, Ti, Ta, W, Al) added to improve its high temperature properties.

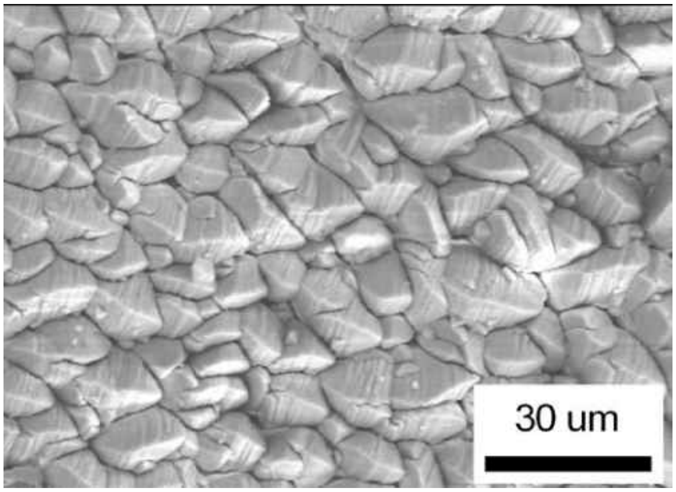

Figure 32: Secondary electron micrograph of the surface of the as-coated TBCs on CMSX-4 superalloy.

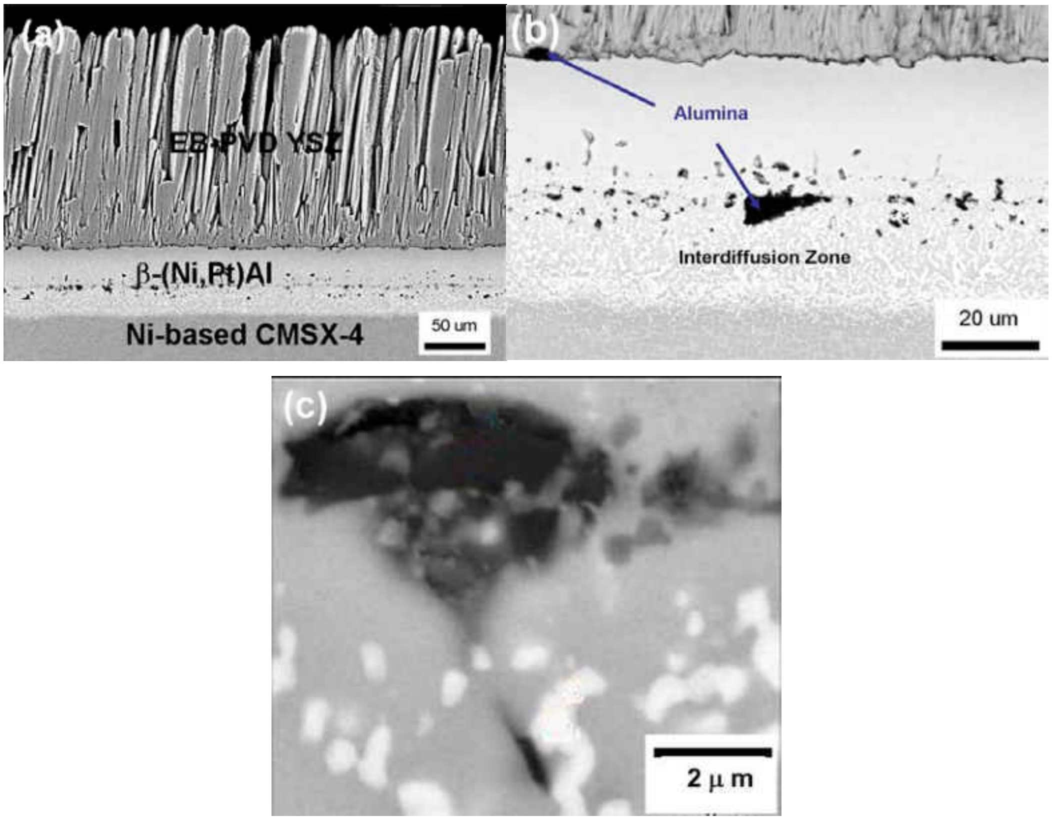

Figure 33: Cross-sectional electron micrographs of the as-coated TBCs with CMSX-4 superalloy: (a) layer structure of EB-PVD TBCs; (b) and (c) show the imperfections at the bond coat/YSZ interface and bond coat/superalloy interface from grit blasting.

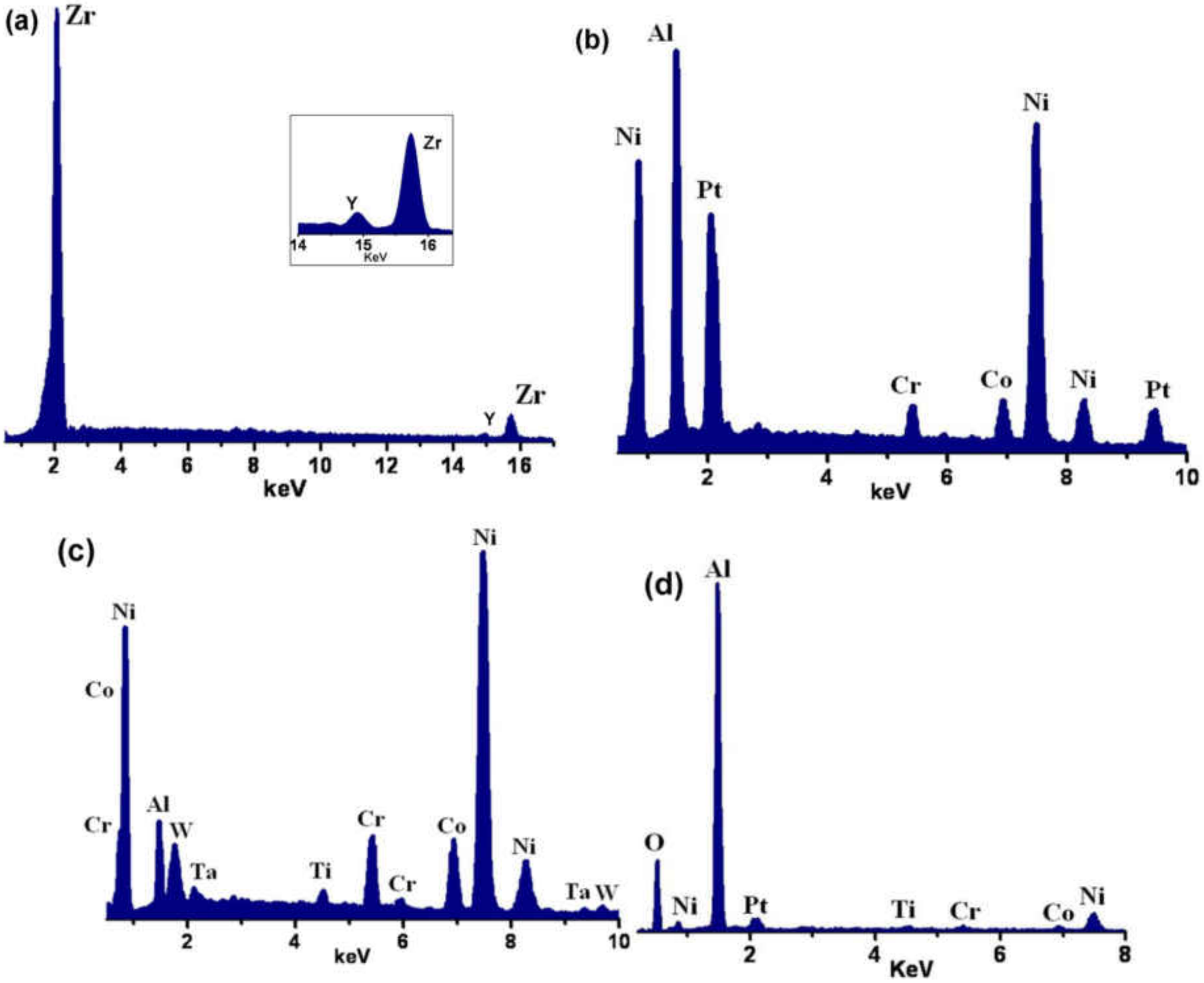

Figure 34: The characteristic EDX spectra of different regions: (a) YSZ top coat, (b) (Ni, Pt)Al bond coat, (c) Ni-based CMSX-4 superalloy and (d) embedded Al_2O_3 from grit blasting.

5.1.2 Lifetime of EB-PVD TBC Specimens

Three of the EB-PVD TBC specimens were thermally cycled at 1100°C with 1 hour dwell. Their individual thermal cyclic lifetimes and the average thermal cyclic lifetime with standard deviation is reported in Table 2 and Figure 35. The lifetime ranged from 740 to 756 cycles. The average lifetime was estimated to be 745 ± 9 cycles. Small standard deviation is observed.

Table 2. Lifetime assessment of disc-shape EB-PVD TBC specimens with CMSX-4 superalloy substrate thermally cycled with 1 hour dwell time at 1100°C.

Specimen label	a	b	c	Average lifetime (hrs)	Standard deviation (hrs)
Thermal cyclic lifetime (hrs)	740	740	756	745	9

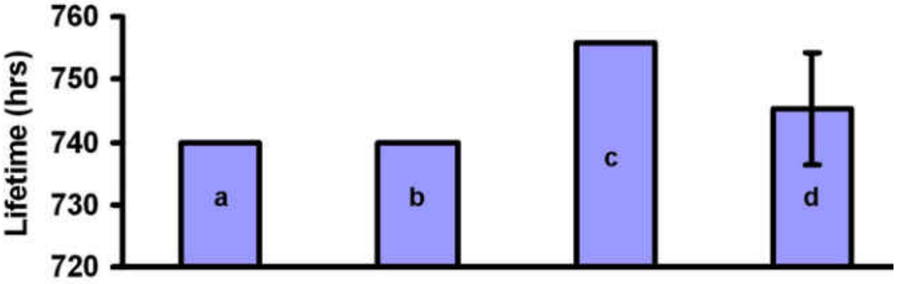

Figure 35: Lifetime of three disc-shape specimens (a, b, c) and the average lifetime along with the standard deviation (d).

5.1.3 Characteristics of Failure

5.1.3.1 Macroscopic Observation

Optical photographs of EB-PVD TBC specimen before and after failure are shown in Figure 36(a) & Figure 36(b) respectively. The specimen was considered to be failed when more than 70% of the coating spalled. The failed specimen, shown in Figure 36(b), has exposed metallic surface and fragments of the remaining coating. The optical photograph of the failed TBC depicts large scale buckling as the mode of failure.

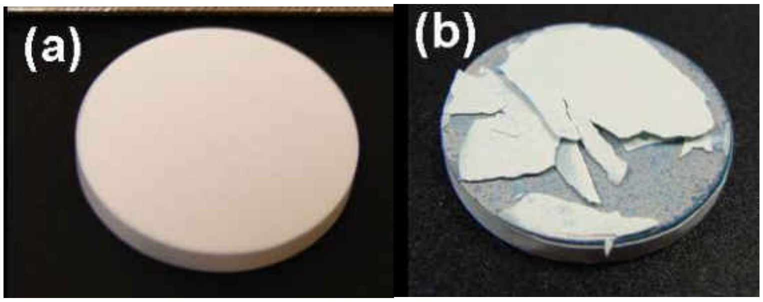

Figure 36: Macro photographs of (a) as-coated EB-PVD TBC specimen with CMSX-4 and (b) failed specimen illustrating the failure mode of TBC.

5.1.3.2 Microstructural Constituents of Fractured Surfaces

Figure 37 shows the optical photograph of failed EB-PVD TBC specimen indicating the two regions: (a) surface of the bare bond coat and (b) the underside of the spalled YSZ, used for compositional analysis to understand the mode of failure. The back-scattered electron micrographs of the exposed surface of the (Ni, Pt)Al bond coat and the underside of the detached YSZ coating are shown in Figure 38(a) & Figure 38(b). The underside of the spalled YSZ has some areas with small domains of TGO; this indicates that failure occurred at the interface between the YSZ and TGO. However the bare surface of the bond coat is not completely covered with TGO and has small sections of metallic bond coat. This indicates that YSZ probably started separating initially, but final failure occurred in a mixed mode. That is along the interfaces of TGO and YSZ, TGO and bond coat; and through TGO.

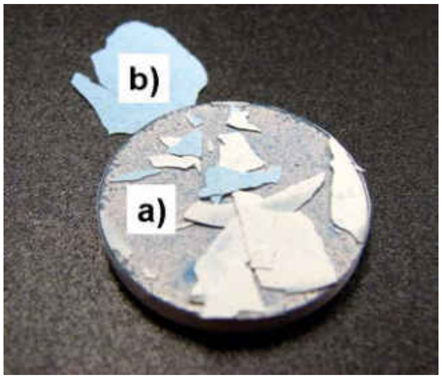

Figure 37: Optical photograph of the failed EB-PVD TBC specimen showing the surfaces, (a) and (b), studied using back-scattered electron microscopy to understand the mode of failure.

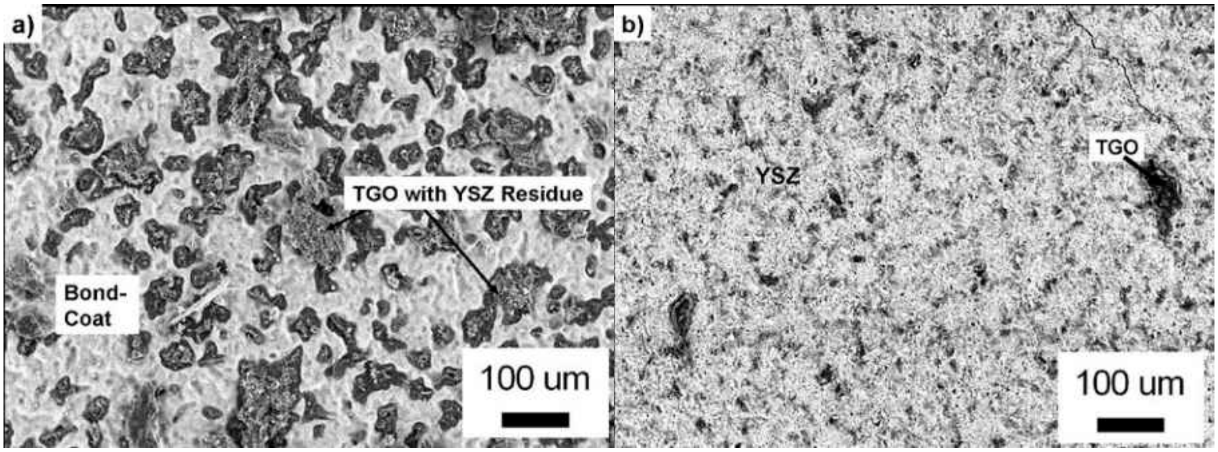

Figure 38: Back-scattered electron micrographs of failed EB-PVD TBC specimen: (a) the surface of the bare bond coat and (b) the underside of spalled YSZ.

5.1.4 Microstructural Degradation

5.1.4.1 Microstructural Changes in the Bond Coat

The elemental composition of the (Ni, Pt)Al bond coat in the as-coated TBC and after oxidation of 224 hours are compiled in Table 3. The back-scattered electron micrograph of the cross-section of TBC around 30% lifetime is shown in Figure 39. Selective oxidation of Al, and interdiffusion between the (Ni, Pt)Al bond coat and the Ni-based superalloy at the peak temperature (1100°C) formed light colored phase. EDX spectra of the lighter region and the dark region are shown in Figure 40(a) and Figure 40(b) respectively. This illustrates high Al content in the dark region, β-NiAl(B2) phase, compared to the lighter region, γ'–Ni_3Al ($L1_2$) phase.

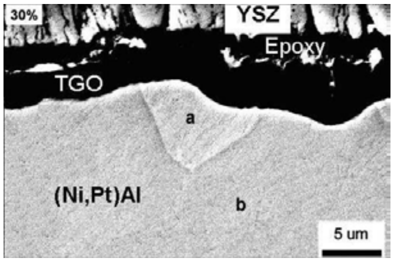

Figure 39: Back-scattered electron micrograph of cross-section of EB-PVD TBC specimen after 224 hours of 1-hr thermal cycling at 1100°C. This depicts patches of (a) *γ'*-Ni_3Al ($L1_2$) phase in the (b) *β*–NiAl (B2) phase near the TGO.

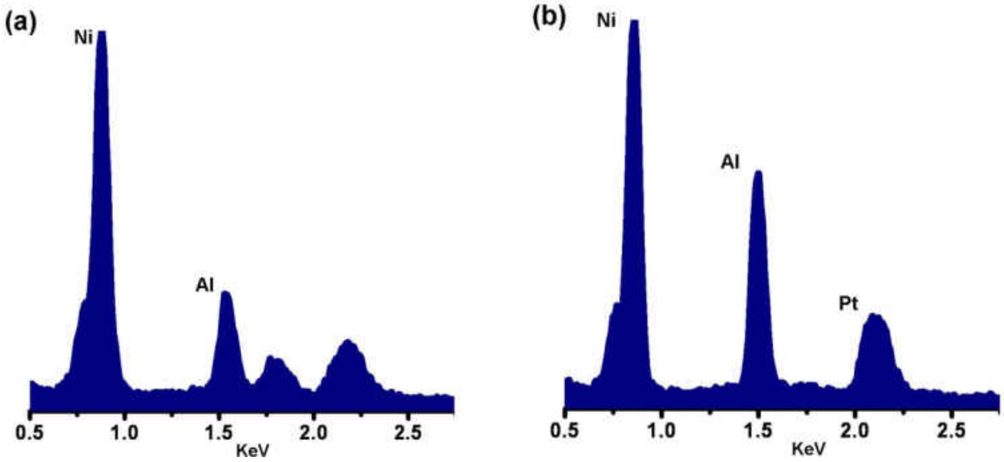

Figure 40: The characteristic EDX spectra of two phases: (a) *γ*''-Ni_3Al and (b) *β*-NiAl, formed in the bond coat of EB-PVD TBC specimen after 224 hours of 1-hr thermal cycling at 1100°C.

Table 3. Composition of (Ni, Pt)Al bond coat in the as-coated and 30% lifetime disc-shape EB-PVD TBC specimens.

Disc-shape EB-PVD TBC specimen		(Ni, Pt)Al bond coat composition (atom%)		
		Ni	Al	Pt
As-coated		46	45	9
30% lifetime		64	28	8
30% lifetime	a[†]	78	22	0
	b[‡]	61	31	8

† and ‡ are lighter and dark phases respectively in (Ni, Pt)Al bond coat of disc-shape EB-PVD TBC specimen after 224 hours of thermal cycling.

5.1.4.2 Rumpling Along the TGO/Bond Coat Interface

Typical cross-sectional back-scattered electron micrographs of EB-PVD TBC after 74 hours and 224 hours of thermal cycling, depicting the rumpling at the interface of TGO with bond coat, are presented in Figure 41. Figure 41(a) shows that damage from rumpling initiate along the TGO/YSZ interface, and subsequently with thermal cycling propagate through the TGO shown in Figure 41(b) and Figure 43.

The undulation at the TGO/bond coat interface was quantified using tortuosity. Tortuosity was measured from the ratio of roughened length (L) and the flat length (L_0) of the TGO/bond coat interface as mentioned earlier in the experimental detail. The average magnitude of tortuosity and standard deviation, for the TGO/bond coat interface at different fractions of the TBC life (as-coated, 5%, 10%, 30%, 50%, 80% and failed) are compiled in Table 4 and presented in Figure 42. Surface treatment of the bond coat, prior to the YSZ deposition, using grit blasting process induced a large magnitude of surface roughness (~1.23) in the as-coated sample. Thermal cyclic oxidation initially reduces these features from grit blasting process. Till 10% lifetime, no significant change in rumpling is observed since the presence of YSZ suppresses undulation. As discussed earlier, the YSZ starts separating initially. Therefore around 30% lifetime the magnitude of rumpling starts increasing from 1.15 and reaches 1.25 for the failed sample.

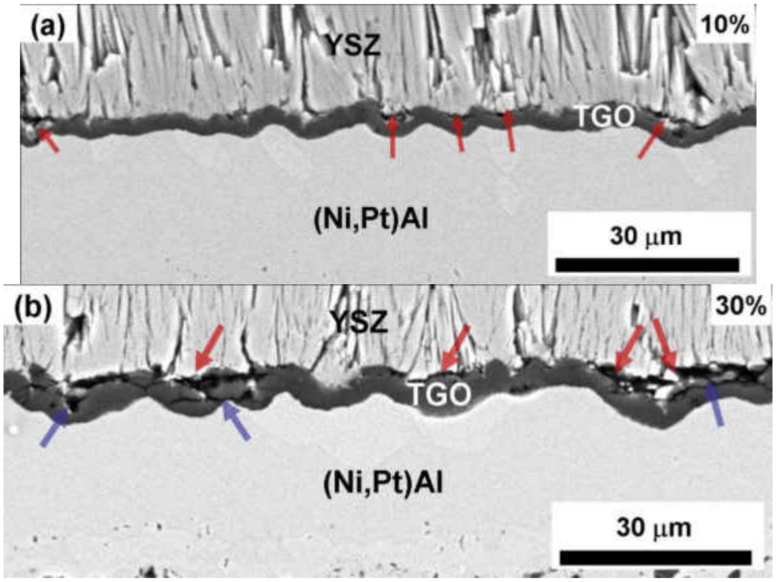

Figure 41: Cross-sectional back-scattered electron micrographs showing the TGO/bond coat interface of EB-PVD TBC specimen after thermal cycling for: (a) 74 cycles and (b) 224 cycles. Red and blue arrows indicate the damages along TGO/YSZ interface and through TGO respectively.

Table 4. Rumpling of the TGO/bond coat interface in disc-shape EB-PVD TBC specimen at different percent of thermal cyclic life.

Percent of thermal cyclic life		0%	5%	10%	30%	50%	80%	Failed
Lifetime of TBCs (cycles)		0	37	74	224	372	596	745
Tortuosity (L/L_0)	Average	1.23	1.14	1.14	1.15	1.17	1.18	1.26
	Standard deviation	0.03	0.03	0.04	0.01	0.03	0.03	0.03

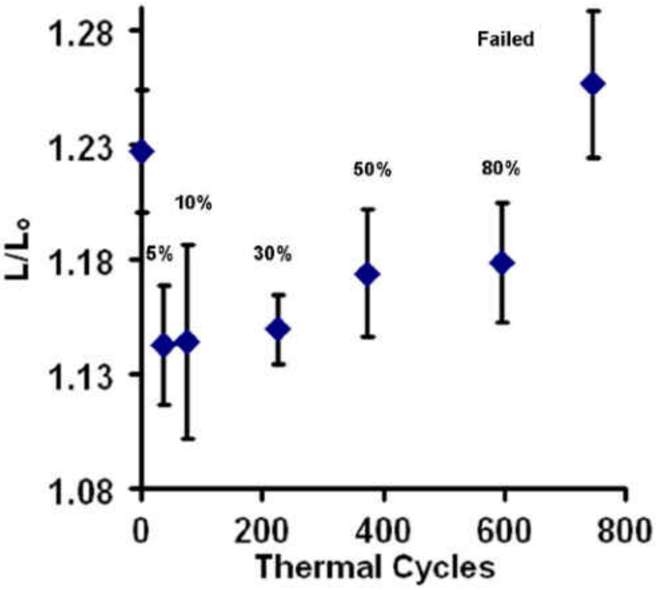

Figure 42: Variation in tortuosity of the TGO/bond coat interface for EB-PVD TBCs with thermal cycling.

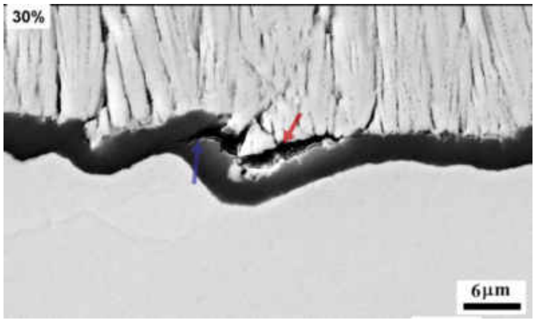

Figure 43: Cross-sectional back-scattered electron micrograph of 30% lifetime EB-PVD TBC depicting the initiation and propagation of damage along the TGO/YSZ interface (shown by red arrow) and through the TGO (shown by blue arrow) respectively.

5.1.4.3 TGO Growth

Cross-sectional micrographs at 0%, 5%, 10%, 30%, 50% and 80% lifetime, shown in Figure 44, demonstrate the increase in thickness of the TGO with cyclic oxidation. Average TGO thickness along with standard deviation at different fractions of the TBC life are listed in Table 5 and presented in Figure 45(a). At the time of failure, the thickness of TGO was ~ 6μm. Oxidation kinetics of the TGO scale was studied by plotting the thickness of the TGO scale with respect to (oxidation time)$^{1/2}$ as shown in Figure 45(b). The parabolic growth rate constant for the TGO in EB-PVD TBC with (Ni, Pt)Al bond coat on CMSX-4 superalloy was found to be 0.19μm/hr$^{1/2}$.

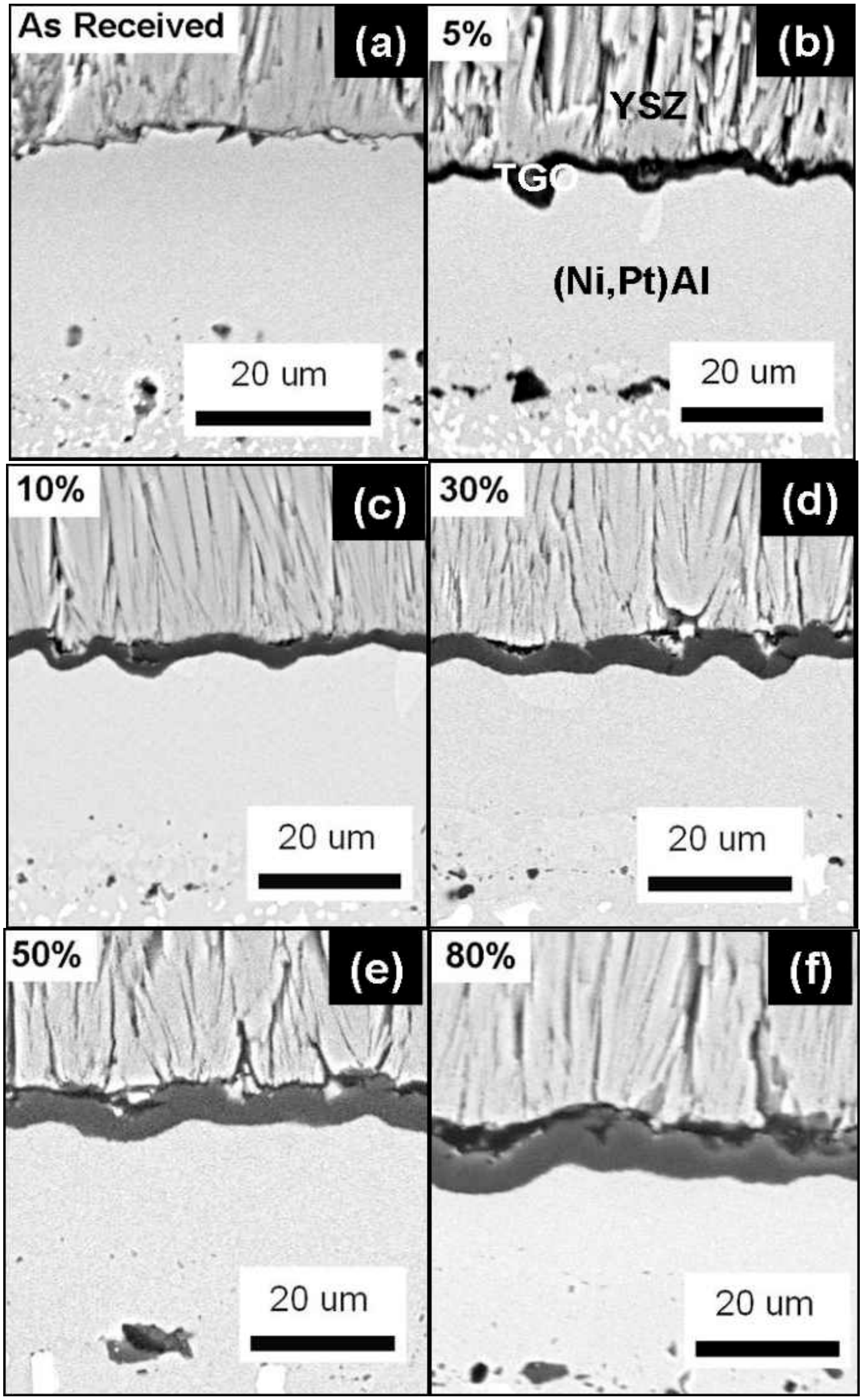

Figure 44: Back-scattered electron micrographs of the TGO scale after (a) 0 cycles, (b) 37 cycles, (c) 74 cycles, (d) 224 cycles, 372 cycles and (e) 596 cycles at 1100°C using 1-hour dwell time.

Table 5. TGO thickness in disc-shape EB-PVD TBC specimen at different percent of thermal cyclic life.

Percent of thermal cyclic life		0%	5%	10%	30%	50%	80%	Failed
Lifetime of TBCs (cycles)		0	37	74	224	372	596	745
TGO thickness (μm)	Average	0.43	1.84	2.68	3.44	4.12	5.22	5.86
	Standard deviation	0.10	0.21	0.27	0.42	0.44	0.65	0.65

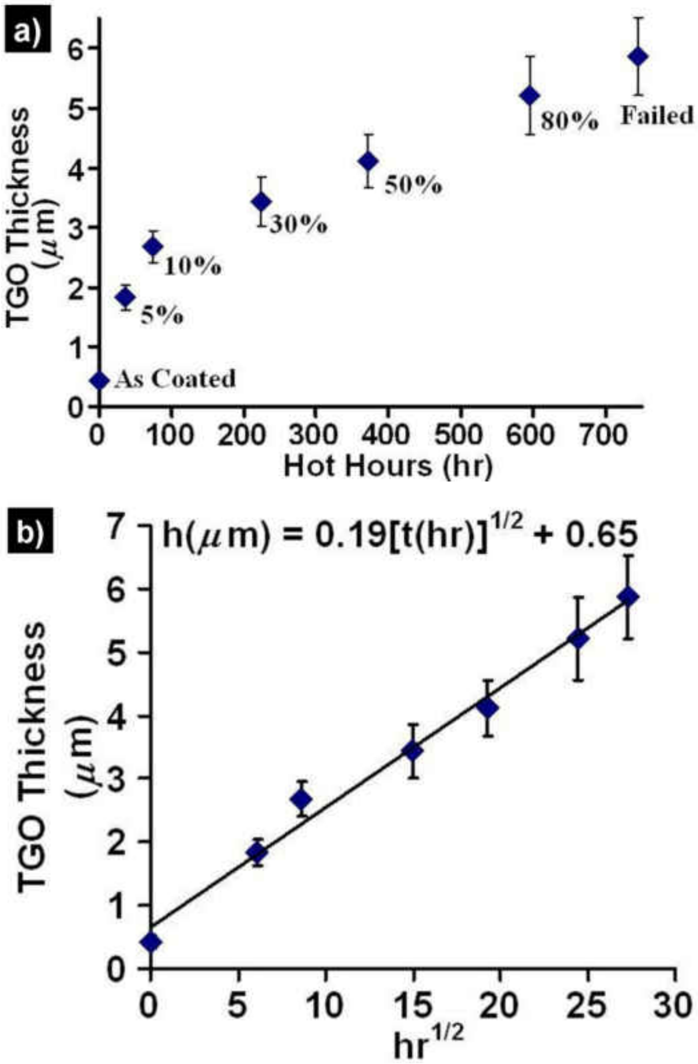

Figure 45: TGO thickness for EB-PVD TBCs as a function of thermal exposure time (a), and the oxidation kinetic (b) at 1100°C.

5.1.5 Residual Stress in the TGO Scale

5.1.5.1 Photostimulated Luminescence Spectroscopy

The presence of compressive residual stress in the TGO scale causes a shift in luminescence spectrum, from the Cr^{3+} impurities present as solid solution in the TGO, relative to the stress free α-Al_2O_3. Figure 46(a) illustrates the shift due to an increase in compressive stress in EB-PVD TBC after 224 thermal cycles. The spectrum generally comprises of a single or multiples of R_1–R_2 doublets. The deconvolution of the spectrum was carried out using peak fitting software, GRAMS 32, and by applying parametric constraints as discussed previously in the experimental detail. Also PLS indicates the phase constituents of Al_2O_3 in TGO. In this study PL spectrum of as-coated sample and those at different stages of oxidation showed the presence of only α-Al_2O_3 in the TGO. Also, all the PL spectra at different fraction of thermal cyclic life comprised of two populations of doublet (R_1–R_2 and R_1'–R_2'), as shown in Figure 46(b). R_1–R_2 and R_1'–R_2' corresponded to high and low compressive residual stress regions in the TGO respectively. Average residual stress values were calculated from the R_2 (high stress) and R_2' (low stress) peak shifts and are listed in Table 6 along with their standard deviations. Figure 47(a) and (b) show the evolution of the peak shift and the corresponding residual stresses, respectively, with thermal cycling. The high and low stresses in the as-coated sample were 2.5GPa and 0.5GPa respectively. Compressive stresses, both high and low, increased with thermal cycling; and after reaching the peak stress of 4GPa & 2.1GPa respectively between 10% to 30% lifetime, started moving towards the stress-free state indicating damages in the TBC.

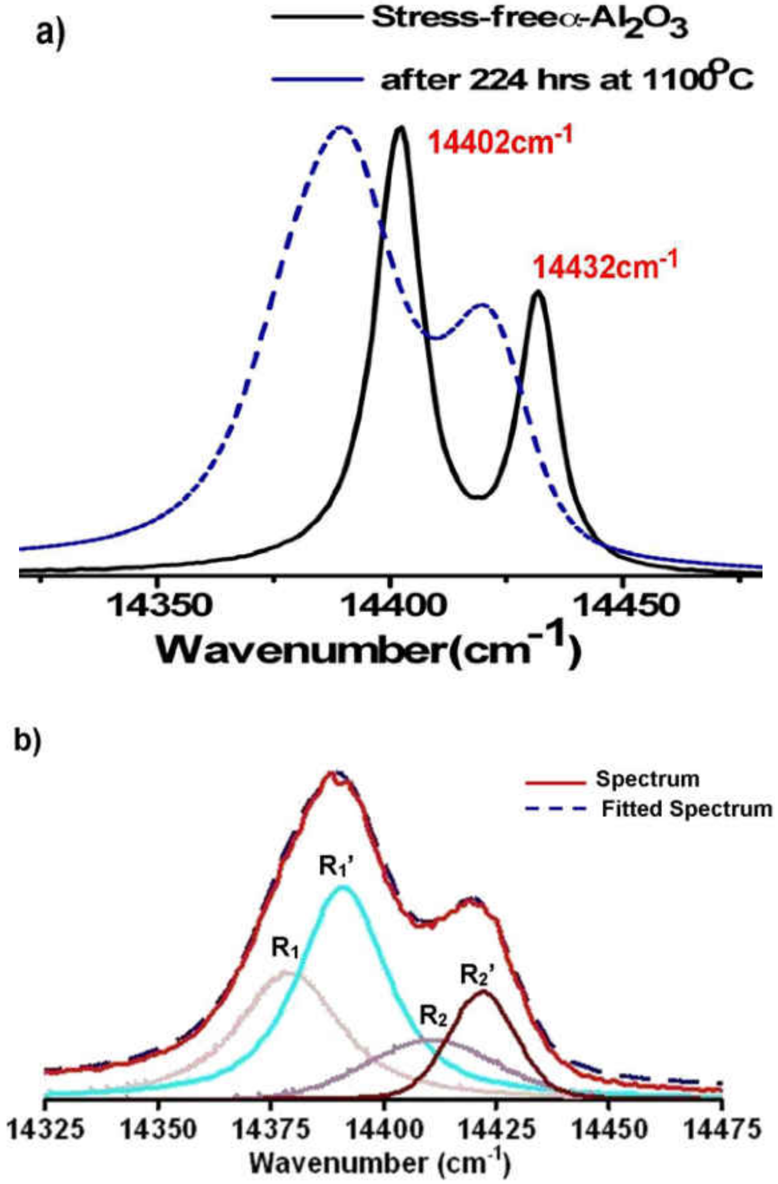

Figure 46: (a) Photoluminescence spectra showing the shift towards lower wave number after thermal exposure for 224hrs at 1100°C of EB-PVD TBC and b) the deconvolution of the PLS curve into two sets of doublet R_1–R_2 and R_1'–R_2'.

Table 6. Compressive residual stress in the α-Al_2O_3 of TGO for disc-shape EB-PVD TBC.

Percent of thermal cyclic life		0%	5%	10%	30%	50%	80%	Failed
Lifetime of TBCs (cycles)		0	37	74	224	372	596	745
High residual stress (GPa)	Average	2.58	3.95	4.08	3..71	2.84	2.88	0.53
	Standard deviation	0.17	0.5	0.62	0.6	0.3	0.47	0.4
Low residual stress (GPa)	Average	0.52	2.09	2.11	2.11	1.36	1.29	0.53
	Standard deviation	0.89	0.16	0.11	0.14	0.3	0.58	0.4

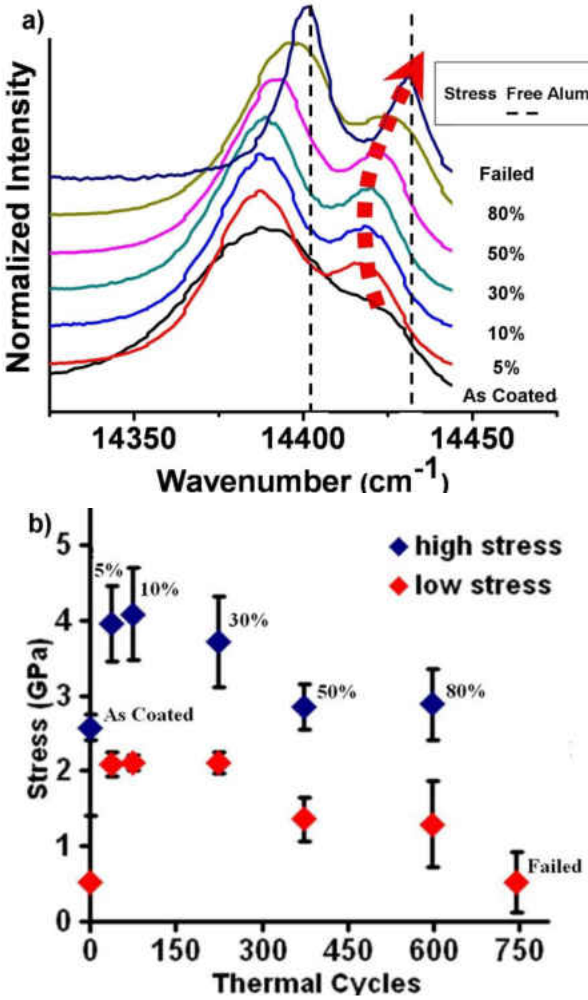

Figure 47: Evolution of a) the PL peak shift, and b) the high and low stresses in the TGO for EB-PVD TBC after: 0 cycles, 37 cycles, 74 cycles, 224 cycles, 372 cycles, 596 cycles and 745 cycles.

5.1.5.2 Correlation to Rumpling

A correlation was observed between the change in compressive residual stress in the TGO scale and the undulation of the TGO/bond coat interface as depicted in Figure 48. Since the low and the high stresses showed similar variations with thermal cycles, to understand the relation with rumpling any one (in this case the high stress) can be employed. The residual stress was found to be inversely related to the tortuosity. With an increase in rumpling from 1.14 to 1.25 the residual stress in the TGO decreased from 4GPa to 0.5GPa.

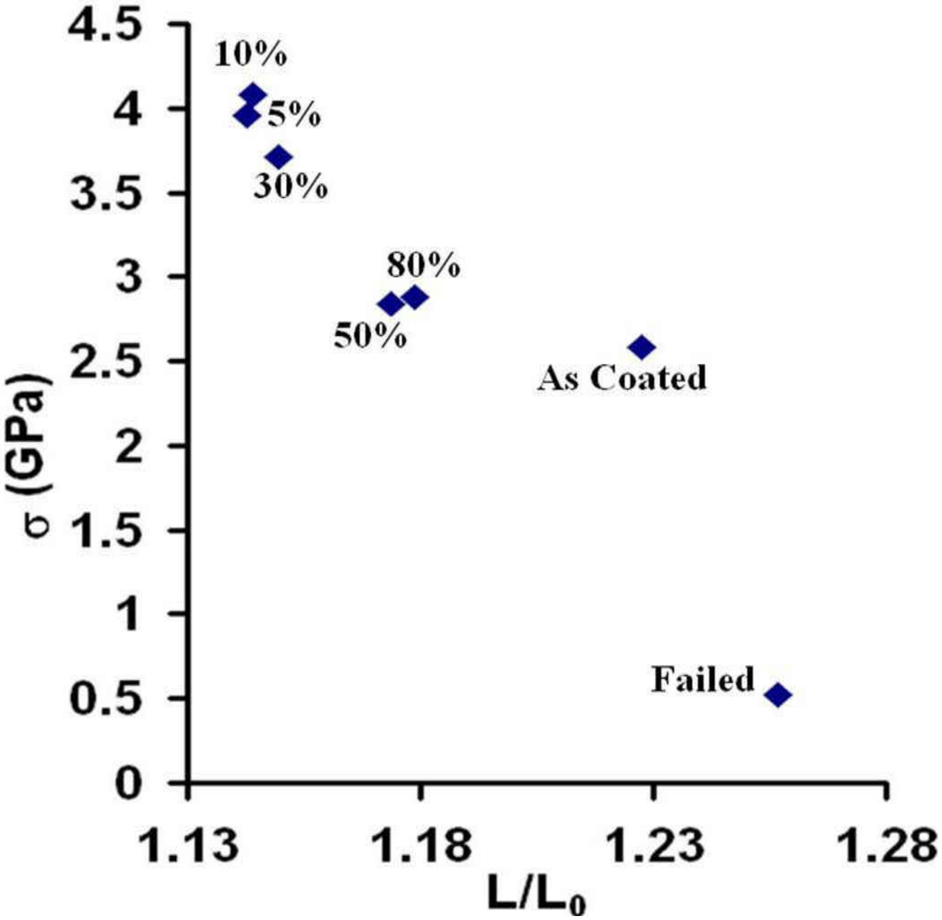

Figure 48: Dependence of in-plane elastic stress in the TGO on the rumpling at the TGO/bond coat interface analyzed along the course of cyclic thermal oxidation.

5.1.6 TGO Energy

As mentioned in chapter 3, the TGO energy was calculated using Eq. (19). TGO energy is a sum of the strain energy in the TGO and the interfacial energy at the TGO/bond coat interface. Eq. (19) shows its dependence on TGO thickness, residual stress in TGO and tortuosity of TGO/bond coat interface. Interfacial, strain and TGO energies at 0%, 5%, 10%, 30%, 50%, 80% lifetime and for the failed sample are presented in Table 7. The interfacial energy and strain energy were individually plotted as a function of thermal cycles as shown in Figure 49(a) and Figure 49(b) respectively. The strain energy increases from 8.5J/m^2 to 128J/m^2. This increase is substantial compared to the interfacial energy term, which shows an increase from 9J/m^2 to 11J/m^2. TGO energy as a function of thermal cycles is shown in Figure 50. The TGO energy was observed to increase rapidly till 10% lifetime and after that it remains almost constant around 135J/m^2 before decreasing to nearly zero as the sample failed. After comparing the trends of the two energy terms with that of the TGO energy, it was found that strain energy mostly governs the trend observed for TGO energy. In the failed TBC, the TGO scale is mostly detached from the bond coat and has very low residual stress (~0.5GPa). This leads to a low magnitude of TGO energy in the failed specimen.

Table 7. Interfacial, strain and TGO energies for disc-shape EB-PVD TBC at different fraction of thermal cyclic life.

Percent of thermal cyclic life	0%	5%	10%	30%	50%	80%	Failed
Lifetime of TBCs (cycles)	0	37	74	224	372	596	745
Interfacial energy (J/m^2)	10.54	9.14	9.16	9.25	9.64	9.73	11.05
Strain energy (J/m^2)	8.52	74.95	116.81	124.99	87.63	128.93	5.16
TGO energy (J/m^2)†	19.07	84.09	125.98	134.24	97.28	138.66	16.21

† TGO energy is the sum of interfacial and strain energies.

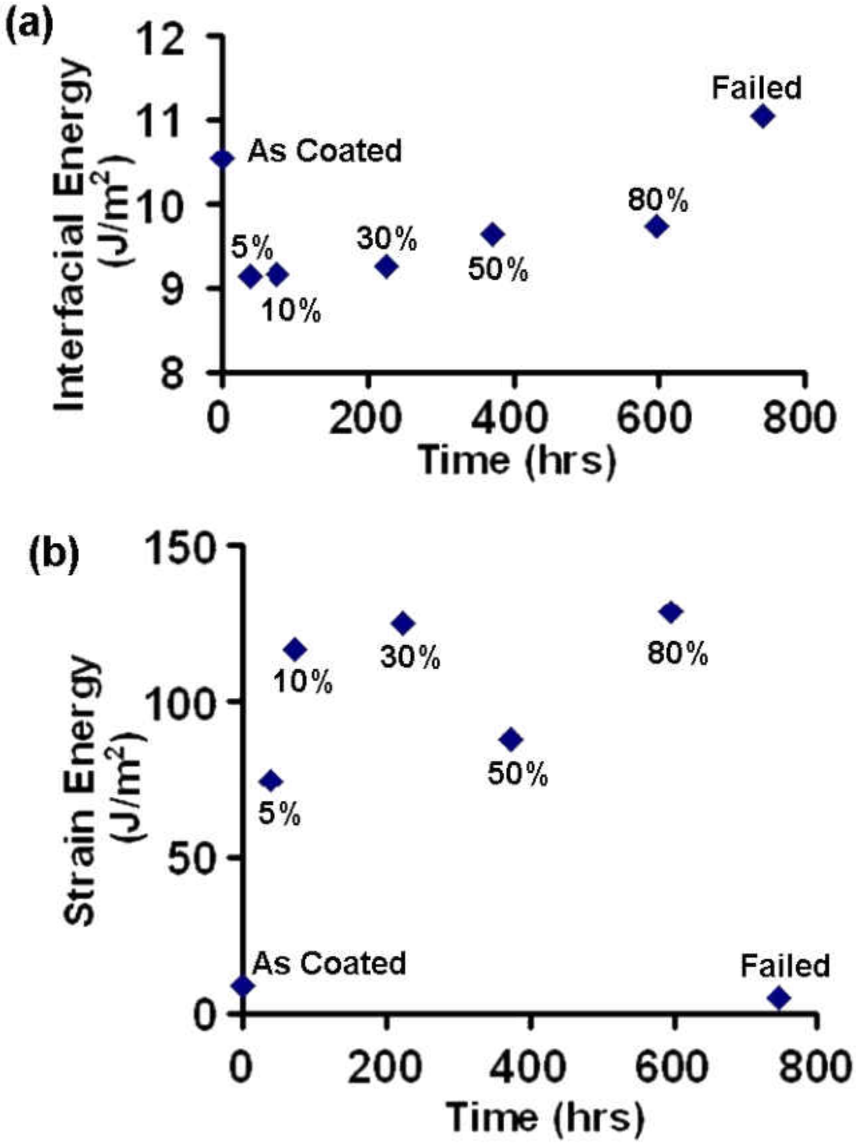

Figure 49: Evolution of (a) interfacial energy at TGO/bond coat interface and (b) strain energy in the TGO for EB-PVD TBC with CMSX-4 substrate with exposure time at 1100°C using 1-hour thermal cycling.

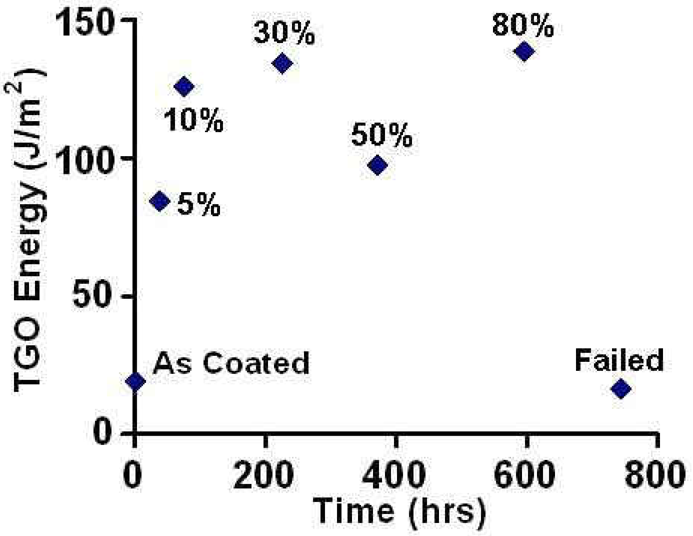

Figure 50: Evolution of TGO energy for EB-PVD TBC with CMSX-4 substrate with exposure time.

5.2 EB-PVD TBCs on High Pressure Turbine Blades

5.2.1 Characterization of As-coated EB-PVD TBC

Figure 51(a) illustrates the inner, mid and outer sections of the as-coated blade. As shown in Figure 51(b) and (c), the portion marked in red was mounted to study the microstructure of the surface and cross-section of the mid-section. The surface morphology of the suction and the pressure side is shown in Figure 52. The pressure side comprise of uniformly distributed fine grains of YSZ. But the suction side has both fine and coarse grains. The cross-sectional back-scattered micrographs in Figure 53(a), (b) and (c) show the top coat has a typical EB-PVD YSZ microstructure with columnar grains separated by channels. The YSZ thickness at the suction side was 153µm, at the pressure side was 135µm and at the leading edge was 146µm. This illustrates non uniform thickness of the YSZ along the blade. The YSZ thickness profile of the entire blade was determined; this will be discussed later. The bond coat was (Ni, Pt)Al on Ni-based superalloy.

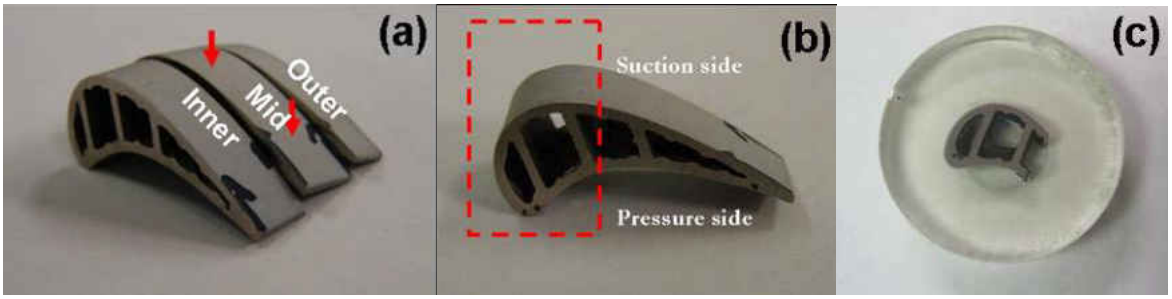

Figure 51: Optical photographs showing (a) the three sections of as-coated blade; (b) the portion (marked in red) of the mid-section used for microstructural study by mounting it in epoxy as shown in (c).

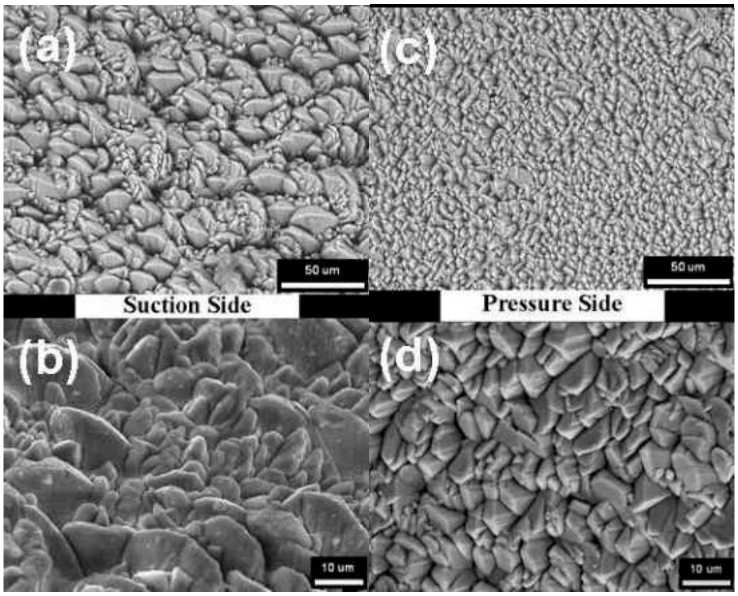

Figure 52: Low and high magnification scanning electron micrographs of surface of the suction side (a) & (b) respectively and the pressure side (c) & (d) respectively, in the mid-section of the as-coated blade.

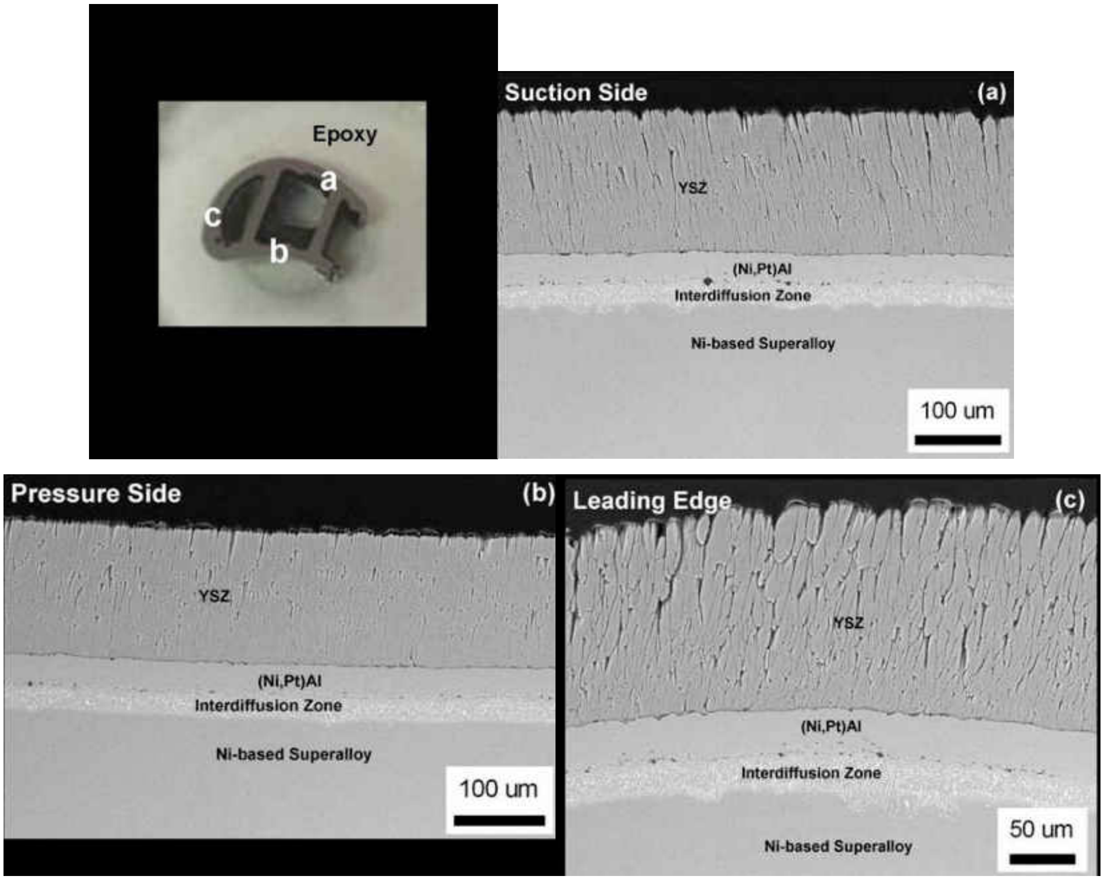

Figure 53: Back-scattered electron micrographs of the cross-section on (a) the suction side, (b) the pressure side and (c) the leading edge.

5.2.2 Characterization of Serviced EB-PVD TBCs

5.2.2.1 Deposits on the Surfaces

Surface secondary electron and cross-sectional back-scattered electron micrographs on the pressure side, suction side and the leading edge of the serviced blade are shown in Figure 54. These micrographs show the presence of deposits throughout the surface of the blade. The composition of the deposit was determined using EDX and is shown in Figure 55. It was found to be rich in Al and contain Ca, Si, Mg, traces of Ti and Fe. No chemical interaction was observed between the deposit and the YSZ top coat.

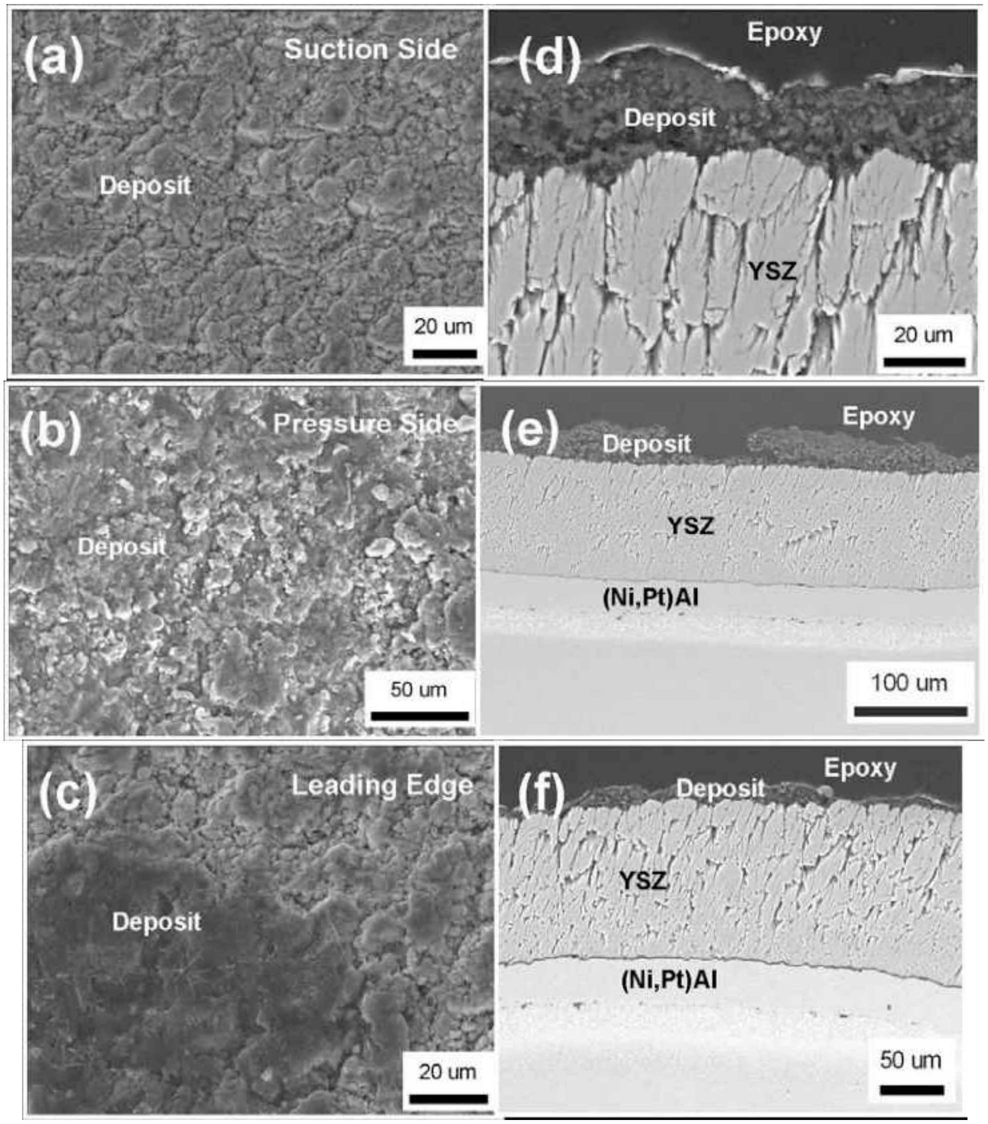

Figure 54: Scanning electron micrographs of the surface on the suction side (a), pressure side (b) and leading edge (c) respectively. Back-scattered electron micrographs of the cross-section on the (d) suction side, (e) pressure side and (f) leading edge, respectively.

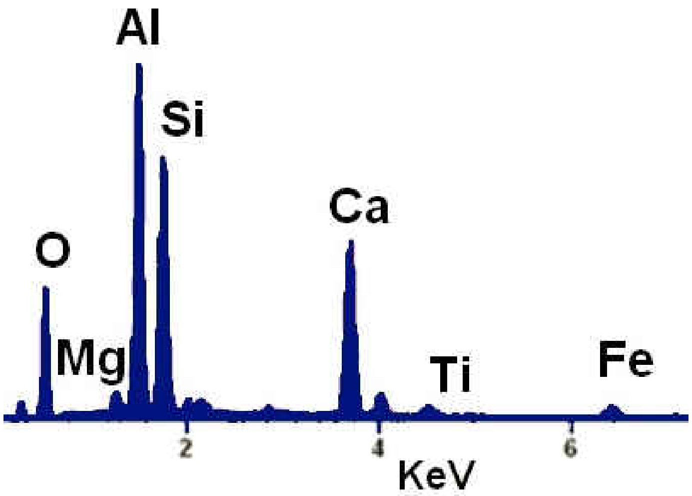

Figure 55: EDX of the deposit on the serviced blade.

5.2.2.2 YSZ Thickness Variation

As mentioned earlier the YSZ thickness in the as-coated blade was not uniform. To preserve the sample for further study, only a small piece of the mid-section of the as-coated blade was used. So the complete YSZ thickness profile could not determined for the as-coated blade. However, the YSZ thickness does not change with oxidation and the thickness profile can be satisfactorily determined from the serviced blade. The YSZ thickness profile of the outer-section of the serviced blade is presented in Figure 56. Average TGO thickness at different regions was calculated using 10 measurements from each of the ten backscattered micrographs taken covering the entire specimen. The top coat thickness ranges from 178μm to 109μm with thicker coating at the leading edge compared to the trailing edge. Also, close to the leading edge, the pressure side had thinner YSZ than the suction side but opposite was observed near the trailing edge.

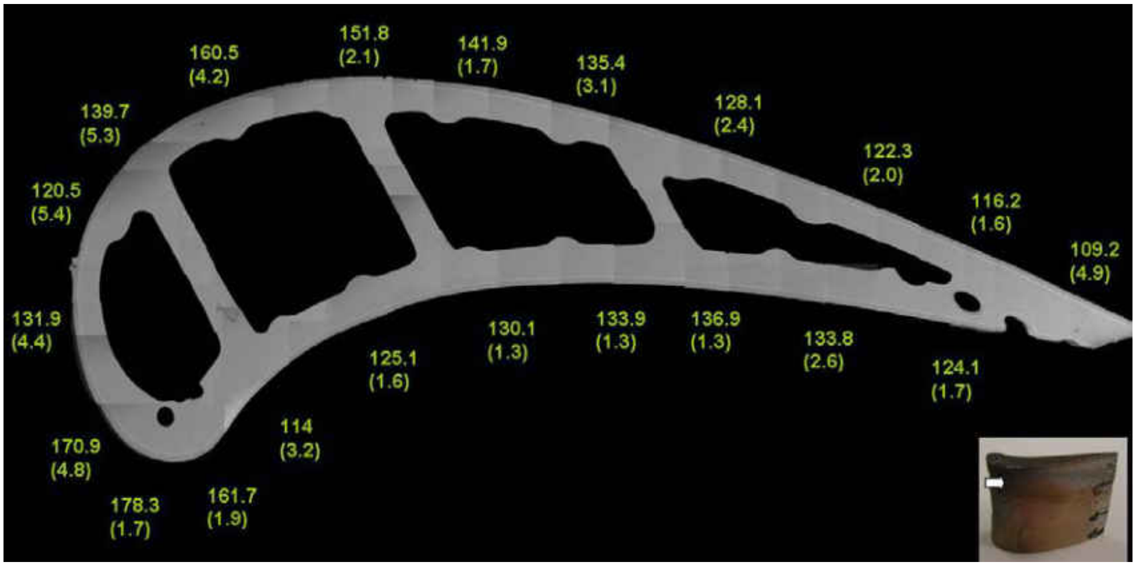

Figure 56: YSZ thickness profile in µm of the outer-section of the serviced blade. The standard deviations are given in parenthesis.

5.2.2.3 TGO Thickness Variation

TGO thicknesses were measured from back-scattered electron micrographs of the cross-sections. The serviced blade has variable TGO thickness throughout the profile of the blade in all of the three sections, shown in Figure 57. All sections of the blade had relatively thick TGO scale at the leading and trailing edges compared to the pressure and suction sides. In the outer-section, the TGO thickness ranges from 0.22µm to 1.15µm. The variation is less in the mid-section, where the TGO thickness ranges from 0.28µm to 1.01µm. In the inner-section the TGO thickness profile has minimum variation that is from 0.21µm to 0.66µm. The peak TGO thickness value at the leading edge increases on moving away from the inner section towards the outer section (from 0.66µm to 1.15µm).

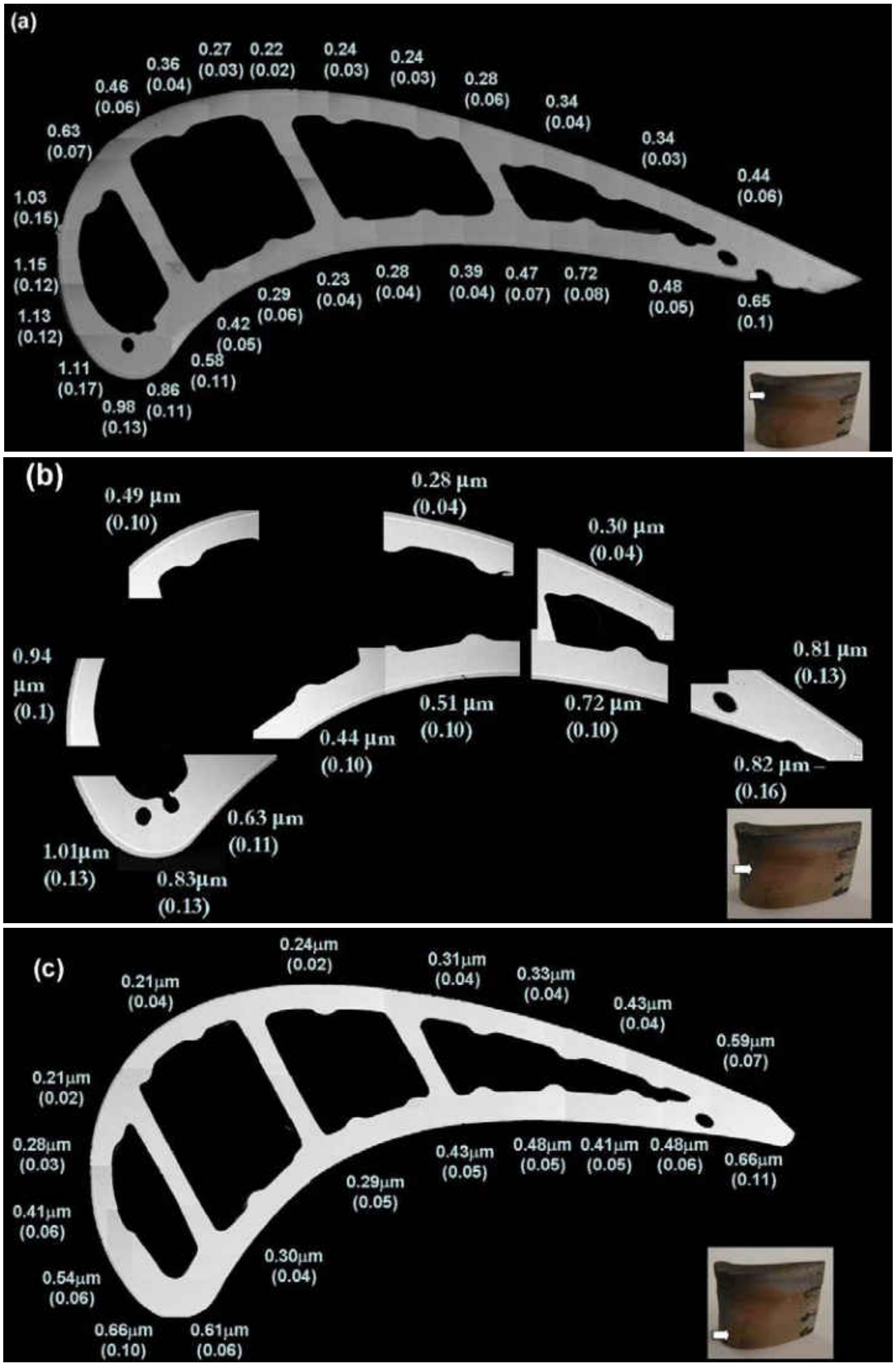

Figure 57: Cross-sectional scanning electron images of the three sections (a) outer section, (b) mid section and (c) inner section of the serviced blade along with their characteristic TGO thickness profiles. Standard deviations are given in parenthesis.

5.2.2.4 Estimated Temperature Distribution

The growth rate constant (k_p) of any TBC depends on temperature and is related using Arrhenius equation given by:

$$k_p = A \times e^{-\frac{Q}{RT}} \tag{21}$$

where A is a pre-exponetial factor, R is the ideal gas constant and Q is the activation energy for oxidation. This relationship for EB-PVD YSZ coated (Ni, Pt)Al bond coat with Ni-based superalloy was established using rate constants at different temperatures from works by other authors [19, 28, 43, 44]. Both the blade and disc-shape TBC (discussed earlier) are same TBC systems with different thermal histories. So the rate constant of disc-shape EB-PVD TBCs from thermal cycling at 1100°C can also be employed to derive the Arrhenius equation. This was estimated by plotting the thickness of TGO as a function of thermal cycling as mentioned earlier in section 5.1.4.3. The rate constants at different temperatures are compiled in Table 8 and presented as a function of temperature in Figure 58. Also, it was observed from the work by S.Sridharan et al. [28] that the rate constant is independent of the dwell time at any given temperature, as k_p of $0.28\mu m/hr^{1/2}$ was reported at 1121^0C for thermal cycling with 1 hour and 24 hour dwell.

Table 8: Parabolic growth rate constants at different temperatures.

	T(^{0}C)	k_p(μm/hr$^{1/2}$)	YSZ thickness (μm)	Dwell time (hr)	Total time (hr)
Present work	1100	0.19	179	1	745
J.Liu	1135	0.24	125	0.83	354
Tolpygo et al.	1150	0.24	125	10	550
Slaxman et al.	1000	0.08	2.5	Isothermal	n.a.
	1000	0.08	27	Isothermal	n.a.
	1000	0.07	80	Isothermal	n.a.
	1050	0.18	2.5	Isothermal	n.a.
	1050	0.17	27	Isothermal	n.a.
	1050	0.16	80	Isothermal	n.a.
	1100	0.27	2.5	Isothermal	n.a.
	1100	0.25	27	Isothermal	n.a.
	1100	0.20	80	Isothermal	n.a.
S.Sridharan et al.	1100	0.25	150	1	1388
S.Sridharan et al.	1121	0.28	150	1	677
S.Sridharan et al.	1151	0.48	150	1	358
S.Sridharan et al.	1121	0.28	150	24	1080

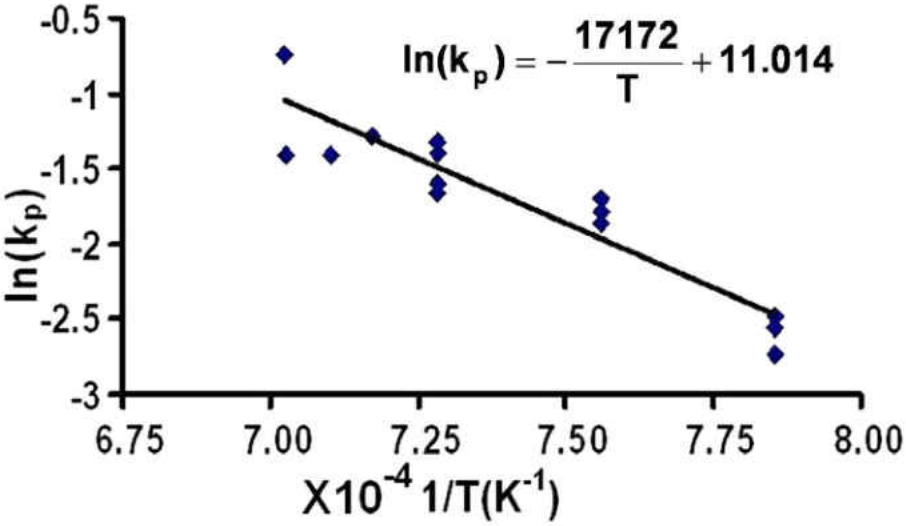

Figure 58: Arrhenius relation of TGO scale growth rate constant for EB-PVD TBCs with (Ni, Pt)Al bond coat on CMSX-4 superalloy.

The relation of growth constant k_p with the thickness of TGO (h) and oxidation time (t) is:

$$k_p = \frac{h-h_0}{t^{1/2}} \tag{22}$$

where h_0 is the average TGO thickness in the as-coated blade and is measured to be 0.23±0.06μm. On substituting Eq. (22) in Eq. (21) and rearranging with experimental data presented in Figure 58, the resulting equation is:

$$T = \frac{17172}{11.014-\ln\left(\frac{h-h_0}{t^{1/2}}\right)} \tag{23}$$

This is the principle equation used for calculating temperature profile at the TGO/bond coat interface. The TGO thicknesses measured in all the three sections along the profile of the serviced blade, previously shown in section 5.2.2.3, were entered for h in Eq. (23) and the service time of 2842 hours was used in for t.

The estimated temperature profiles from Eq. (23) for the three sections of the blade are shown in Figure 59. In all the sections the TGO/bond coat interface at the leading edge experienced high temperature during service compared to other regions of the blade. However the value decreased from 866^0C to 811^0C on moving towards the inner section. Also, pressure side was exposed to higher temperature compared to the suction side. The temperature of the TGO/bond coat interface at the trailing edge for all the sections was higher than the centre of the blade but lower than their respective temperatures at the leading edge.

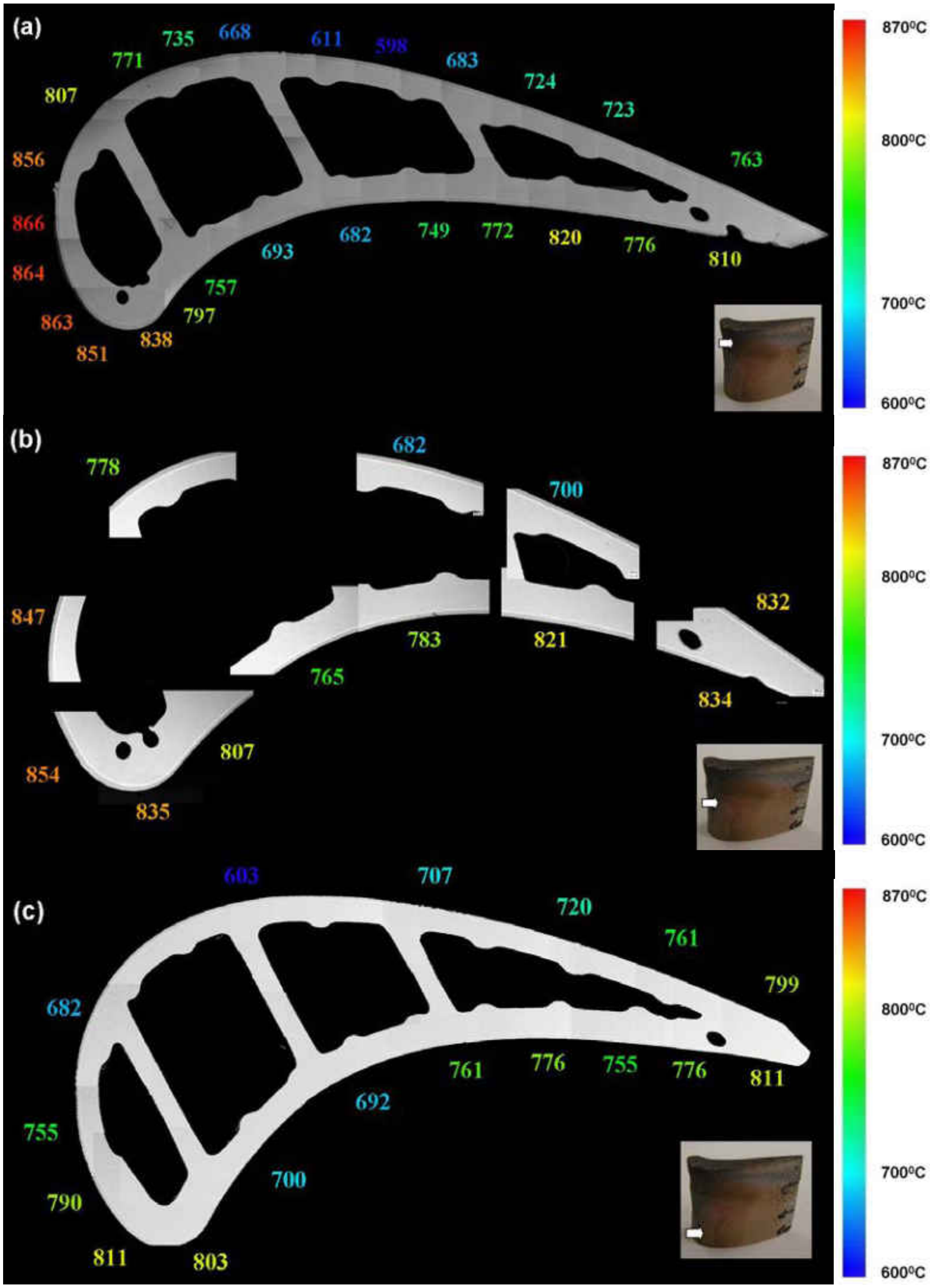

Figure 59: Temperature (^{0}C) profile of (a) outer section, (b) mid section and (c) inner section.

5.2.3 Residual Stress in the EB-PVD TBCs on Blades

5.2.3.1 As-coated Blade

The PLS spectrum was deconvoluted into two sets of doublets similar to disc-shape EB-PVD TBCs. Two populations of stress, high stress and low stress were calculated using the shifts of R_2 and R_2' peaks respectively, relative to the stress-free value 14432cm^{-1}. The average values of high and low stresses in the TGO at the pressure side are 4.1±0.2GPa and 1.4±0.1GPa respectively. The average values of high and low stresses in the TGO at the suction side are 3.7±0.3GPa and 0.8±0.4GPa respectively. The residual stress can depend on the curvature of the blade and the pressure side has higher value of stress compared to the suction as shown in Figure 60.

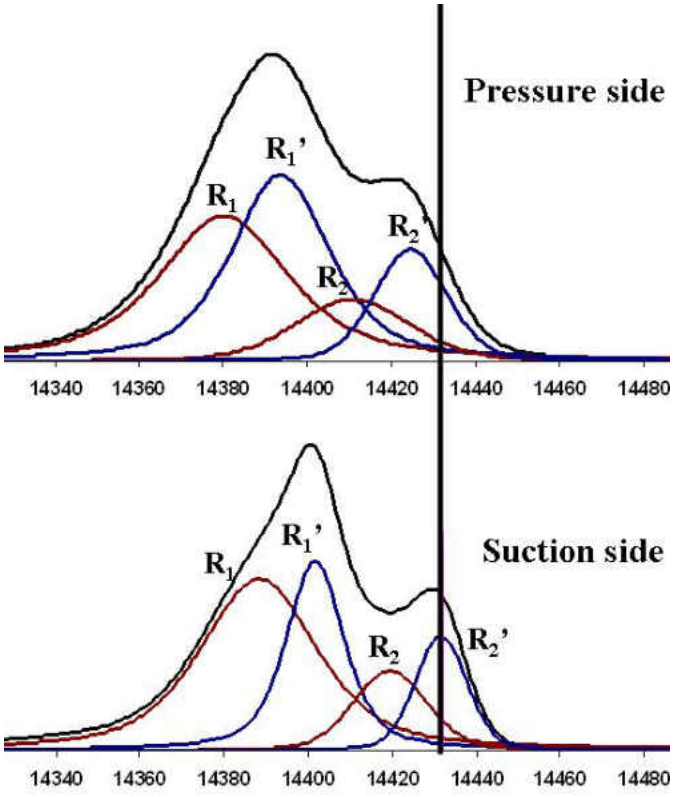

Figure 60: PLS spectrum at the pressure side (a) and the suction side (b) of the as-coated blade.

5.2.3.2 Serviced Blades

Residual stress measurement could not be performed on the serviced blades due to the presence of thick layer of deposit, illustrated before in section 5.2.2.1 using electron micrographs and EDX, which gave stress free peaks due to the presence α-Al_2O_3 on deposits.

CHAPTER 6 DISCUSSION

6.1 Failure Mechanism in the Disc-Shape EB-PVD TBCs

Failure mode for the EB-PVD TBCs with grit blasted (Ni, Pt)Al bond coat on CMSX-4 superalloy could not be solely characterized by examining the back-scattered images of the bare bond coat surface in Figure 38(a) and the underside of the spalled YSZ Figure 38(b). The latter shows small domains of TGO indicating failure along the TGO and YSZ interface. However the former has relatively large fraction of TGO but not entirely covered with it, indicating that the fracture also occurred within the TGO.

To understand the origin and propagation of fracture and failure mode, more detail study on the cross-section of the EB-PVD TBCs at different fractions of life was carried out. The cross-sectional back-scattered electron micrographs in Figure 41(a) shows that at 10% lifetime cracks originate at the YSZ and TGO interface due to rumpling of the TGO and the TGO/bond coat interface. With further thermal cycling the amplitude of undulation increases and for TBCs with 30% life, damages propagate into the TGO and along the TGO/bond coat interface. The rumpling may have caused the formation of tensile stress at the crest and facilitated separation between the bond coat and TGO. Finally the cracks coalesce and TBC fails by large scale buckling. So the final failure of the EB-PVD TBCs with (Ni, Pt)Al bond coat occurs in a mixed mode.

A rough interface has larger interfacial area, consequently interfacial energy, compared to a flat interface. Any system tries to minimize its energy but Figure 42 shows that the roughness, measured using tortuosity, increases with thermal cycling. So, the question arises why the surface roughens. This can possibly be answered from the PLS study on the TBCs that measures the residual stress in the TGO scale.

Residual stresses arise in the absence of any external force when there is a thermal gradient in a material or when two materials with different thermal expansion coefficients are inter-connected. This occurs in pair, i.e. tensile stress in one area causes compressive stress in an adjacent area. The thermal expansion coefficient of TGO is $8\text{x}10^{-6}{}^{\circ}\text{C}^{-1}$ and that of the bond coat is $14\text{x}10^{-6}{}^{\circ}\text{C}^{-1}$. This induces compressive residual stress in the TGO after every cycle on cooling from the peak temperature and consequently tensile stress in the bond coat. Also the TGO grows at peak temperature, with a rate constant $0.19\mu\text{m/hr}^{1/2}$, which produces a low magnitude of compressive stress in the TGO. At high temperature, residual stress may be relieved by other phenomena like yielding and creep in the TGO. The net residual stress, a combination of growth stress and thermal mismatch stress, measured at room temperature increases with cyclic oxidation time as shown in Figure 47(b) until around 10% to 30% lifetime. At 10% lifetime TBCs have cracks only along the YSZ/TGO interface and this has little effect on minimizing the residual stress in the TGO. However after oxidation till 30% lifetime, cracks are observed through the TGO and along the TGO/bond coat interface. This should cause the residual stress in the TGO to decrease significantly. Also, deconvolution of the PLS spectrum into two sets of peaks shows non uniform stress in the TGO throughout the thermal cyclic life. This can possibly arise from the non-planar TGO scale due to rumpling at the interface.

A correlation was also observed between the rumpling of TGO/bond coat interface and the residual stress in the TGO. Even though rumpling increases the interfacial energy in the TBC with thermal cycle, it reduces the residual stress as shown in Figure 48. The residual stress and consequently the elastic strain energy in the TGO is the fundamental driving force for the failure in TBCs. A decrease in residual stress, with thermal cycling, however by itself cannot explain the TBC failure. To explain this both the interfacial energy and the elastic strain energy were combined in Eq. (19) as TGO energy. These two energies were considered, because the damages (within TGO and along TGO/bond coat interface) incurred from thermal cycling will release these energies and subsequently form free surfaces having characteristic surface energies. When released energy is greater than the surface energy created, the process will be spontaneous.

The elastic strain energy was calculated using the high stress value. The high stress value represents the elastic strain in the area of the TGO with minimal damage. The interfacial energy calculated from the tortuosity measurements has trend similar to the tortuosity as shown in Figure 49(a). Its variation with oxidation time is not significant. The variation in elastic strain energy with time, shown in Figure 49(b) mostly determines the nature of TGO energy variation with oxidation time. The evolution of TGO energy with thermal cycling was determined to understand its contribution to the final failure. Figure 50 shows that the TGO energy reaches a peak value of ~135J/m^2 around 30% lifetime when cracks start forming in the TGO and TGO/bond coat interface.

It has been already discussed that rumpling decreases the residual stress. To understand the effect of rumpling around this peak energy, from 10% lifetime to 80% lifetime, variation in residual stress with rumpling was plotted for the TGO thickness values of 1μm, 3μm and 5μm using the following equation:

$$\sigma = \sqrt{\left(\frac{135(\mathrm{J/m^2})}{\left(\frac{\mathrm{L}}{\mathrm{L_0}}\right)^2} - \gamma_{\mathrm{MO}} \right) * \frac{\mathrm{E}}{(1-\nu)\mathrm{h}}} \tag{24}$$

Eq. (24) was obtained by substituting 135J/m^2 for TGO energy and rearranging Eq. (19). The thickness range was chosen such that it includes the measured thicknesses of TGO in disc specimen of EB-PVD TBCs from 10% to 80% lifetime. Figure 61 shows that rate of decrease in the residual stress as a function of rumpling reduces with an increase in the TGO thickness.

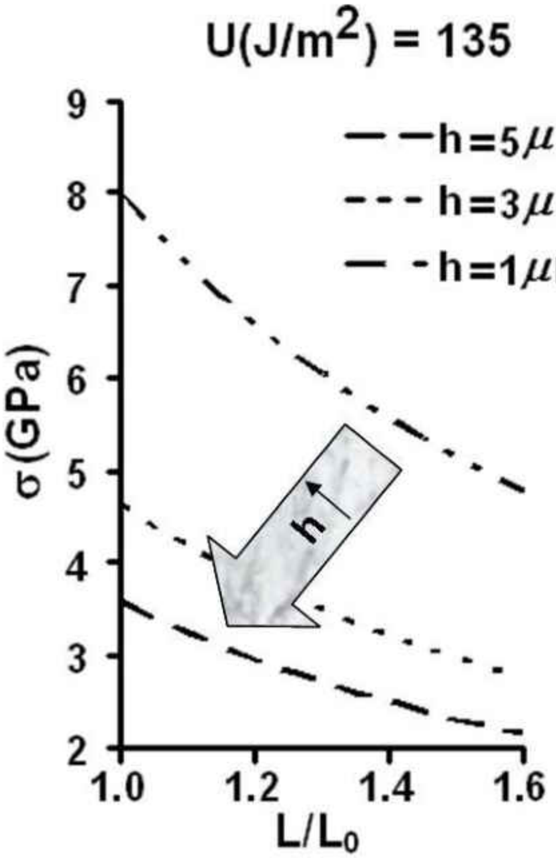

Figure 61: Variation in residual stress in the TGO with rumpling at the TGO/bond coat interface. The TGO energy is held constant at 135J/m^2 and TGO thickness is 1μm for the upper curve, and is incremented uniformly to 5μm.

To validate the conclusion derived from Figure 61, the residual stresses and rumpling data measured at 10%, 30% and 80% lifetime were plotted in the above graph. This is shown in Figure 62. The measured TGO thickness for 10%, 30% and 80% lifetime TBCs lies within the TGO thickness range used for the analytical study, so any conclusion derived from Figure 61 is reasonable.

Table 9. TGO thickness and residual stress in the disc-shape EB-PVD TBC specimen at 10%, 30% and 80% thermal cyclic life.

Percent of thermal cyclic life	10%	30%	80%
Lifetime of TBCs (cycles)	74	224	596
TGO thickness (μm)	2.68	3.44	5.22
Residual stress (GPa)	4.08	3.71	2.88
Rumpling (L/L_0)	1.14	1.15	1.18

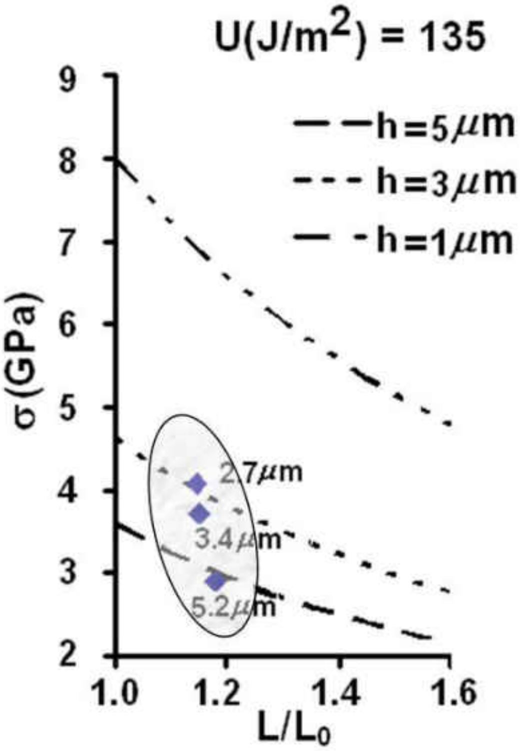

Figure 62: Comparison of the experimental results for 10%, 30% and 80% lifetime EB-PVD TBCs with analytical estimate.

6.2 Thermal Exposure of EB-PVD TBCs on High Pressure Turbine Blade

The high pressure turbine blades are close to the turbine inlet and experience very high temperature and pressure compared to the low pressure turbine blades. The efficiency of the turbine depends on the temperature of the compressed air around the blade and there is a need to measure this temperature accurately. A traditional method is to back-calculate from the measured temperature of the exhaust gas. However this gives only the average value and is not very accurate. Other methods used are thermal crystals, thermal paint and thermocouples. These methods give temperature profile of the surface of the blade. In this study the temperature profile at the interface of the YSZ and bond coat was determined using the growth rate of the oxide at different regions of the blade. This temperature will depend on the thermal conductivity (k/Wm^{-1}K^{-1}) of the YSZ, surface temperature, thickness of the YSZ and heat flux (q/Wm^{-2}) given by Fourier's law:

$$q = \frac{k\left(\mathrm{T_{surface}}\text{-}\mathrm{T_{interface}}\right)}{\mathrm{h_{YSZ}}} \tag{25}$$

The heat flux and thermal conductivity are assumed constant. If the ambient temperature at the surface is assumed to be uniform then the $\mathrm{T_{interface}}$ will be higher for regions with thinner YSZ. So the trailing edge should have higher $\mathrm{T_{interface}}$ than the leading edge, but in all the sections of the serviced blade the leading edge has higher $\mathrm{T_{interface}}$. This shows that the surface temperature profile of the blade is not uniform and will be higher at the leading edge. The YSZ thickness at the leading edge of the three sections of the serviced blade is assumed the same. Higher $\mathrm{T_{interface}}$ at the leading edge of the outer section indicates higher surface temperature. Also, the center region for all the three sections has lower temperature at the interface. Also, from the PLS on the as-coated blade, the residual stress is higher at the pressure side compared to the suction side.

CHAPTER 7 CONCLUSION

Failure of disc-shape EB-PVD TBC specimens examined in this study using furnace thermal cycling at 1100°C with 1 hour dwell occurred after 745 ± 9 cycles. The back-scattered electron micrographs of the failed sample surfaces, bare bond coat surface and the underside of the spalled YSZ, and cross-sections of TBCs at different fractions of lifetime demonstrated that the damage originated primarily along the YSZ/TGO interface. However the final fracture mode is mixed with damages propagating along the interfaces of the TGO with YSZ and bond coat, and within the TGO leading to failure by large scale buckling.

The growth of TGO scale at 1100°C has a parabolic rate constant of $0.19\mu m/hr^{1/2}$. The TGO scale reached a thickness of $\sim 6\mu m$ close to the final failure. The rumpling at the TGO/bond coat interface increased with thermal cycling and the tortuosity ranged from 1.15 to 1.25. Compressive residual stress in the TGO scale increased initially and gradually decreased with thermal cycling, and ranged from 2.5 to 4.0GPa. An inverse relation was observed between the compressive residual stresses and rumpling showing the contribution of rumpling in reducing the stress in the TGO scale. An equation relating the TGO energy with the scale thickness, residual stress and rumpling was defined. A parametric study showed that the contribution of rumpling in residual stress reduction decreased with an increase in TGO thickness.

High pressure turbine blade had a non uniform thickness profile for the YSZ coating. Also, the YSZ grain sizes varied throughout the blade; the pressure side mostly had fine grains of YSZ and the suction side had both fine and coarse grains. The pressure side of the as-coated blade had higher residual stress compared to the suction side; the difference may be due to the curvature of the blade. The serviced blade was covered with a thick layer of deposit, comprising of Al, Ca, Si, Mg, Ti and Fe. This hindered residual stress measurement, and mostly gave stress-free peaks from the α-Al_2O_3 within the deposit. All three sections (inner, mid and outer) of the serviced blade had non uniform TGO thickness profile that also varied between the sections. Using the Arrhenius relation derived from the work on disc-shape EB-PVD TBCs and by other authors on EB-PVD TBCs with grit blasted (Ni, Pt)Al bond coat on CMSX-4 superalloy, the interfacial temperature profiles for the three sections of the blade were determined. The leading edge and the trailing edge experienced higher interfacial temperature compared to pressure side and the suction side. The leading edge had higher interfacial temperature compared to the suction side; this contradicted the assumed temperature based on the YSZ thickness profile indicating a non uniform temperature at the blade surface. The interfacial temperature at the leading edge decreased from the outer section to the inner section.

REFERENCES

1. G. W. Goward, and D. H. Boone, Oxid. Met. **3**, 475 (1971).

2. N. P. Padture, M. Gell, and E. H. Jordan, Science **296**, 280 (2002).

3. A. G. Evans et al., Prog. Mater. Sci. **46**, 505 (2001).

4. A. G. Evans, M. Y. He, and J. W. Hutchinson, Prog. Mater. Sci. **46**, 249 (2001).

5. J. S. Smith and D. H. Boone, 'Platinum modified aluminides – present status', Paper 90-GT-319, Gas Turbine and Aeroengine Congress, New York, NY, ASME, 1990.

6. H. G. Scott, J. Mat. Sci. **10**, 1527 (1975).

7. R. A. Miller, Surf. Coat. Technol. **30**, 1 (1987).

8. W. D. Kingery, J. Am. Ceram. Soc. **38**, 3 (1955).

9. S. Stecura, "Optimization of the NiCrAl- Y/ZrO2-Y2O3 thermal barrier system" NASA Tech. Memo. 86905, NASA, Cleveland OH.

10. E. C. Subbarao, in Science and Technology of Zirconia, A. H. Heuer, L. W. Hobbs, Eds. (American Ceramic Society, Columbus, OH, 1984), vol. 3, p. 1.

11. D. P. H. Hasselman, Am. Ceram. Soc. Bull. **66**, 799 (1987).

12. O. Unal, T. E. Mitchell, and A. H. Heuer, J. Am. Ceram. Soc. **77**, 984 (1994).

13. M. J. Stiger et al., Zeitschrift für Metallkunde **90**, 1069 (1999).

14. M. W. Brumm, and H. J. Grabke, Corros. Sci. **33**, 1677 (1992).

15. J. Doychak, and M. Rühle, Oxid. Met. **31**, 431 (1989).

16. J. Doychak, J. Smialek, and T. Mitchell, Metall. Mater. Trans. A **20**, 499 (1989).

17. M. W. Brumm, and H. J. Grabke, Corros. Sci. **34**, 547 (1993).

18. J. P. Roux, and H. J. Grabke, Appl Surf Sci **68**, 49 (1993).

19. S. Laxman et al., Surf. Coat. Technol. **177-178**, 121 (2004).

20. U. Schulz et al., Surf. Coat. Technol. **146-147**, 117 (2001).

21. V. K. Tolpygo, D. R. Clarke, and K. S. Murphy, Metall. Mater. Trans. A **32**, 1467 (2001).

22. D. Monceau et al., J. Mater. Res. **15**, 665 (2000).

23. L. Xie et al., Surf. Coat. Technol. **176**, 57 (2003).

24. I. T. Spitsberg, D. R. Mumm, and A. G. Evans, Mat. Sci. Eng. A-Struct. 394, 176 (2005).

25. D. M. Lipkin, and D. R. Clarke, Oxid. Met. **45**, 267 (1996).

26. L. Grabner, J. Appl. Phys. **49**, 580 (1978).

27. A. Selçuk, and A. Atkinson, Acta Mater. **51**, 535 (2003).

28. S. Sridharan et al., Surf. Coat. Technol. **179**, 286 (2004).

29. J. He, and D. R. Clarke, J. Am. Ceram. Soc. **78**, 1347 (1995).

30. Q. Ma, and D. R. Clarke, Acta Metall. Mater. **41**, 1817 (1993).

31. V. K. Tolpygo, and D. R. Clarke, Acta Mater. **46**, 5153 (1998).

32. A. A. Kaplyanskii, A. K. Przhevuskii, and R. B. Rozenbaum, Sov. Phys. Solid State **10**, 1864 (1969).

33. H. J. Grabke et al., Oxid. Met. **35**, 199 (1991).

34. P. K. Wright, and A. G. Evans, Curr. Opin. Solid State Mater. Sci. **4**, 255 (1999).

35. M. Y. He, A. G. Evans, and J. W. Hutchinson, Mat. Sci. Eng. A-Struct. **245**, 168 (1998).

36. V. K. Tolpygo, and D. R. Clarke, Mat. Sci. Eng. A-Struct. **278**, 151 (1999).

37. J. W. Hutchinson, M. Y. He, and A. G. Evans, J. Mech. Phys. Solids **48**, 709 (2000).

38. J. Dundurs, J. Appl. Mech. **36**, 650 (1969).

39. A. G. Evans, M. Y. He, and J. W. Hutchinson, Acta Mater. **45**, 3543 (1997).

40. M. Y. He, A. G. Evans, and J. W. Hutchinson, Acta Mater. **48**, 2593 (2000).

41. D. Lynch, JOM **61**, 41 (2009).

42. J. L. Smialek and G. H. Meier, High-temperature oxidation, in Superalloys II, Eds. C. T. Sims, N. S. Stoloff, and W. C. Hagel, Wiley, 1987.

43. V. K. Tolpygo, D. R. Clarke, and K. S. Murphy, Surf. Coat. Technol. **146-147**, 124 (2001).

44. J. Liu, Ph.D. Dissertation, University of Central Florida, Fall 2007.

45. E. Schumann *et al.*, Oxid. Met. **53**, 259 (2000).

46. A. M. Karlsson, J. W. Hutchinson, and A. G. Evans, J. Mech. Phys. Solids **50**, 1565 (2002).

47. D. S. Balint, and J. W. Hutchinson, J. Mech. Phys. Solids **53**, 949 (2005).

48. J. W. Hutchinson, and Z. Suo, Adv. Appl. Mech. **29**, 63 (1991).

49. V. K. Tolpygo, and D. R. Clarke, Acta Mater. **47**, 3589 (1999).

50. A. M. Karlsson, and A. G. Evans, Acta Mater. **49**, 1793 (2001).